



**UNIVERSITY OF LEEDS**

This is a repository copy of *Impact breakage of acicular crystals*.

White Rose Research Online URL for this paper:

<http://eprints.whiterose.ac.uk/156550/>

Version: Accepted Version

---

**Article:**

Saifoori, S, Goh, W-P, Ali, M et al. (1 more author) (2020) Impact breakage of acicular crystals. *Powder Technology*, 361. pp. 651-662. ISSN 0032-5910

<https://doi.org/10.1016/j.powtec.2019.11.061>

---

© 2019 , Elsevier. This manuscript version is made available under the CC-BY-NC-ND 4.0 license <http://creativecommons.org/licenses/by-nc-nd/4.0/>.

**Reuse**

This article is distributed under the terms of the Creative Commons Attribution-NonCommercial-NoDerivs (CC BY-NC-ND) licence. This licence only allows you to download this work and share it with others as long as you credit the authors, but you can't change the article in any way or use it commercially. More information and the full terms of the licence here: <https://creativecommons.org/licenses/>

**Takedown**

If you consider content in White Rose Research Online to be in breach of UK law, please notify us by emailing [eprints@whiterose.ac.uk](mailto:eprints@whiterose.ac.uk) including the URL of the record and the reason for the withdrawal request.



[eprints@whiterose.ac.uk](mailto:eprints@whiterose.ac.uk)  
<https://eprints.whiterose.ac.uk/>

# Impact Breakage of Acicular Crystals

Saba Saifoori, Wei-Pin Goh, Muzammil Ali, Mojtaba Ghadiri\*  
School of Chemical and Process Engineering, University of Leeds, Leeds, UK

\*Contact email: [m.ghadiri@leeds.ac.uk](mailto:m.ghadiri@leeds.ac.uk)

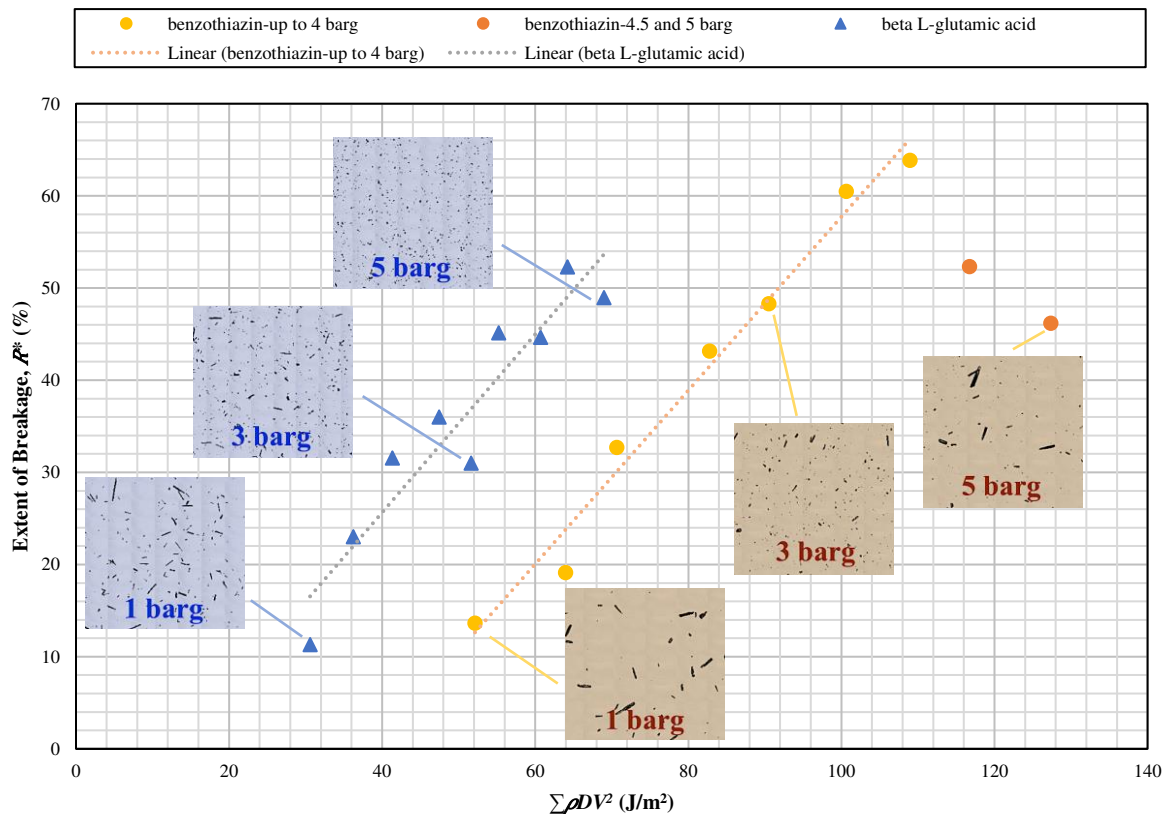
## Highlights

- Impact breakage of acicular crystals by aerodynamic dispersion is analysed.
- Dispersion is achieved by an air pressure pulse using Morphologi G3.
- Impact velocity against walls is related to pulse pressure by CFD.
- Shift in particle size distribution is used to estimate breakage extent.
- Dependence of breakage extent on velocity is used to infer breakability.

## Abstract

Acicular crystals are frequently encountered in pharmaceutical and fine chemical industries. They are prone to breakage, as a result of which their bulk behaviour changes drastically. It is therefore of great interest to be able to assess their breakage propensity quickly and preferably using a small quantity. An integrated experimental and modelling method is proposed to quantify the breakability of acicular crystals by aerodynamic dispersion using the disperser of Morphologi G3, in which a pulse of compressed gas induces particle impact. Needle-shaped crystals of  $\beta$  L-glutamic acid, benzothiazin and potassium phosphate are used as the model test materials. The extent of breakage as a function of dispersion pressure is obtained by quantifying the shift in particle size distribution provided by Morphologi G3. It increases as the dispersion pressure is increased for  $\beta$  L-glutamic acid and benzothiazin particles, while not noticeably for potassium phosphate crystals. The impact velocity of the particles at different pressures is estimated by computational fluid dynamics (CFD) calculations. Its effect on the extent of breakage is used to infer the ease with which the crystals break, expressed by a lumped parameter as the ratio of hardness over square of toughness. Benzothiazin breaks by fracture along both crystal length and width due to presence of cleavage planes, whilst  $\beta$  L-glutamic acid breaks only perpendicular to the length. Potassium phosphate undergoes minor chipping from the edges and corners.

1 Graphical Abstract: Impact Breakage of Acicular Crystals Due to  
 2 Aerodynamic Dispersion by a Compressed Air Pressure Pulse  
 3



4  
 5 **Keywords**

6 Breakage; acicular; aerodynamic; dispersion; Morphologi G3; impact; crystals; attrition

7  
 8 **1. Introduction**

9 A wide range of industrial processes involve processing and handling of particulate solids like  
 10 crystals, granules and agglomerates. Particle breakage may be induced desirably as in milling  
 11 or undesirably by attrition, thereby altering particle properties, namely size distribution, shape,  
 12 surface area, and other physical and chemical attributes, such as dissolution. Particularly in  
 13 chemical and process industries, the operation and economy of manufacturing processes are  
 14 affected by such changes [1]. Breakage can negatively affect the quality and characteristics of  
 15 the product and the function of the equipment, as well as the environment due to dust formation,  
 16 but it can also positively affect the manufacturing process, e.g. by increasing the crystallisation  
 17 rate through increasing the number of nuclei available for crystallisation [2].

1 Breakage by impact is commonly encountered in a wide range of process equipment, such as  
2 fluidised beds, cyclones, stirred vessels [3], and of course in milling operations. Here our focus  
3 is on powders and grains of particle sizes around a few millimetres or smaller. Early studies  
4 incorporated experimental impact tests, where individual particles were accelerated by air flow  
5 and impacted on a rigid target. These include the works of Yüregir et al. [4,5] with NaCl  
6 crystals, Salman et al. [6,7] with spherical solids and Cleaver et al. [8] with sodium carbonate  
7 monohydrate crystals. Primary research on the impact breakage of agglomerates include the  
8 works of Ning et al. [9] and Boerefijn et al. [10] on  $\alpha$ -lactose monohydrate particles, Subero  
9 and Ghadiri [11] on bonded glass ballotini and Samimi et al. [12] on detergent-based  
10 agglomerates. Additionally, impact attrition of granules has been investigated by Salman et al.  
11 [13], Antonyuk et al. [14] and Dumas et al. [15]. Lecoq et al. [16] employed a test rig of their  
12 own design to impact particles of different materials on a target. They used sieving to analyse  
13 the size distribution of the particles after impact in order to quantify their breakage.  
14 Subsequently, Rozenblat et al. [17] developed a correlation for the breakage kernel and  
15 breakage probability as a function of impact velocity and initial particle size. Lecoq et al. [18]  
16 determined a particle breakage parameter by applying the model of Vogel and Peukert [19] to  
17 particles impacting in an air-jet mill. The model of Vogel and Peukert is based on Weibull  
18 equation [20] describing the failure probability and it is thus applicable to the brittle failure  
19 mode of particles. There are also several studies on impact particle breakage in the semi-brittle  
20 mode, in particular the works of Ghadiri and Zhang [21], Samimi et al. [22], Subero-Couroyer  
21 et al. [23] and Olusanmi et al. [24], where a lumped parameter, describing the breakability, as  
22 expressed by the ratio of hardness over square of toughness, has been quantified for a wide  
23 range of materials. More recently, Bonakdar et al. [25] evaluated the suitability of Scirocco  
24 disperser of Malvern Panalytical Mastersizer 2000 as a device for testing breakability of  
25 crystalline solids by using an integrated experimental and CFD modelling approach, the latter  
26 analysed by Ali et al. [26]. They observed that a unification of breakage data could be obtained  
27 when the relative change in the surface area was expressed as a function of particle size, density  
28 and velocity. Using the extent of breakage obtained from a single particle impact test, Bonakdar  
29 et al. [27] had a similar observation for burkeite particles.

30

31 Most of the studies on impact breakage of particles address the failure of equant-shaped  
32 crystals, granules, agglomerates, etc. There is scant coverage of breakage related to acicular  
33 (needle-shaped) particles in the literature. In fact, most of the studies on acicular particles  
34 revolve around their breakage under compaction. For instance, Grof et al. [28] simulated the

1 breakage of needle-shaped particles during uniaxial compaction using discrete element method  
2 (DEM). Their computational studies revealed that the presence of both strong and weak  
3 particles in the mixture resulted in a more significant fragmentation for the weaker ones. It was  
4 also observed that mixtures containing both strong and weak particles tend to experience larger  
5 extents of breakage compared to mixtures consisting of particles with a narrow range of  
6 strength. Also, in the latter case, longer particles tended to break at lower compaction ratios  
7 compared to shorter ones. Following that, Grof et al. [29] developed and validated a  
8 methodology to determine the breakage kernel and daughter particles length distribution  
9 functions for needle-shaped crystals by combining computational and experimental techniques  
10 using DEM and population balance modelling (PBM). They proposed that using this  
11 methodology, a single-pass uniaxial compaction experiment would be sufficient for predicting  
12 the extent of breakage and suggested simulation of other stressing modes, such as impact, as  
13 the first step for future research. In a more recent work, Guo et al. [30] used DEM to develop  
14 a model for predicting the breakage of high aspect ratio particles in an agitated bed. They  
15 observed that the breakage rate increased with an increase in pressure, impeller rotational  
16 speed, interparticle and particle-equipment friction. They validated the model using  
17 experimental results obtained from breakage of chalk sticks subjected to uniaxial compression.  
18

19 There have also been studies in which breakage is analysed during processes where acicular  
20 particles fail due to both impact and shear. MacLeod and Muller [31] showed that the breakage  
21 of needle-shaped crystals occurs during both pressure filtration and agitated drying steps. They  
22 developed a qualitative model of breakage for particles in a filter bed using particle dimensions,  
23 applied pressure and bed density. Also, for the drying steps, where they considered the  
24 breakage to be due to impact rather than compression, they suggested the implementation of  
25 Ghadiri and Zhang [21] model for prediction of breakage. Also, Ho et al. [32] carried out ball  
26 milling of acicular crystals of D-mannitol and used dynamic image analysis (DIA) and inverse  
27 gas chromatography (IGC) to explain their breakage trends. They concluded that a combination  
28 of attachment energy prediction and particle shape and surface energy characterisation is  
29 necessary to explain the breakage behaviour of crystalline solids in milling. Last but foremost,  
30 the work of Antonyuk et al. [33] is the sole study where acicular particles are investigated for  
31 their breakage caused by impact. They used a new electromagnetic particle gun that enabled  
32 collision of single acicular L-threonine crystals with a wall under predefined impact angle and  
33 velocity. Sieving was employed to obtain a characteristic length for the particles. They

1 compared their experimental results with DEM analysis of breakage and showed good  
2 agreement.

3

4 Considering the above-mentioned literature, impact breakage during handling of acicular  
5 particles, especially in case of micron-sized crystals, still remains poorly characterised.  
6 Therefore, this topic is addressed in this work by a combination of experimental impact testing,  
7 using Malvern Panalytical Morphologi G3 disperser and CFD simulations for calculating the  
8 impact velocity. The objective is to first explore the suitability and applicability of Morphologi  
9 G3 disperser as an impact breakage test device, and then to quantitatively characterise the  
10 breakability of various acicular crystals due to impact with the walls of the dispersion spool.  
11 To this end, acicular crystals of three test materials are dispersed by Morphologi G3 at different  
12 pressure pulses and their extent of breakage is determined by quantifying the shift in the particle  
13 size distribution, analysed using the Morphologi G3 microscope and image analysis system.  
14 Then, three-dimensional multiphase computational fluid dynamic simulations of the dispersion  
15 chamber of Morphologi G3 are carried out to calculate the particle trajectories and impact  
16 velocities induced by the compressed air pulse. The extent of breakage along with the  
17 calculated impact velocity of the particles in the instrument are then used to determine the  
18 breakability of the test particles.

19

## 20 2. Methodology

21

### 22 2.1 Experimental

23 Crystals of  $\beta$  L-glutamic acid, benzothiazin (2H-1, 4-benzothiazin-3 (4H)-one, 97%) and  
24 potassium phosphate monobasic are used as the model test particles as they have an acicular  
25 shape. Scanning electron microscopy (SEM) images of the shapes are shown in Fig. 1, taken  
26 by Hitachi TM3030 tabletop microscope (Hitachi Ltd., Tokyo, Japan). The densities of the  
27 model test particles are  $1600 \text{ kg/m}^3$  for  $\beta$  L-glutamic acid [34],  $1197 \text{ kg/m}^3$  for benzothiazin  
28 [35] and  $2340 \text{ kg/m}^3$  for potassium phosphate [36]. In this work, the crystals of  $\beta$  L-glutamic  
29 acid have been crystallised from water, while benzothiazin and potassium phosphate crystals  
30 have been obtained from Sigma-Aldrich and Fluorochem, respectively. The breakage of these  
31 crystals is analysed using Morphologi G3 (Malvern Panalytical Ltd., Worcestershire, UK),  
32 which has a dispersion system and an optical microscope with a built-in software package used  
33 to measure the morphological characteristics of particles.

34



1  
2 Fig. 1. Scanning electron microscopy (SEM) images of:  $\beta$  L-glutamic acid crystals (a); benzothiazin crystals (b); potassium  
3 phosphate crystals (c).

4  
5 The dispersion chamber of the instrument consists of a dispersion capsule with a spool, into  
6 which a small amount of sample (typically a few  $\text{mm}^3$ ) is placed. A pulse of compressed air  
7 with adjustable pressure and duration of 20 ms is injected into the dispersion chamber. The  
8 particles are then dispersed by the air pressure pulse, impacting onto the walls of the dispersion  
9 spool causing potential breakage, before leaving it and landing onto a glass slide placed at the  
10 base of the dispersion chamber for microscopy and image analysis. The optical unit then scans  
11 across the dispersed sample on the slide, capturing 2D images of the projected view of  
12 individual particles lying on their plane of maximum stability. Morphologi G3 software  
13 translates the images into a binary format and calculates a range of measures of particle sizes,  
14 such as area, circle-equivalent diameter, length, width, aspect ratio, etc.

15  
16 The experiments are carried out at ten dispersion pressures of 0.5, 1, 1.5, 2, 2.5, 3, 3.5, 4, 4.5  
17 and 5 barg in order to impact the particles at different velocities. Particle breakage is then  
18 analysed by calculating the shift in particle size distribution. Sample size used for each  
19 experiment is  $7 \text{ mm}^3$  for  $\beta$  L-glutamic acid and benzothiazin particles and  $26 \text{ mm}^3$  for  
20 potassium phosphate particles (two sets of  $13 \text{ mm}^3$  samples individually dispersed at each  
21 pressure before the relevant scan is done). A larger sample mass is used for potassium  
22 phosphate crystals in order to compensate for the low particle count per sample, which is  
23 caused by their large size. The experiments are then repeated for a total of three measurements  
24 per dispersion pressure for  $\beta$  L-glutamic acid and benzothiazin particles and five measurements  
25 per dispersion pressure for potassium phosphate particles. Subsequently, in order to increase  
26 the particle count, the particles recorded in each of the measurements corresponding to the  
27 same pressure are combined together for each of the test particles (treating particles obtained  
28 from each of the measurements as fractions of a total sample); this not only increases the

1 representativeness of the sample, but also reduces the fluctuations in the particle size  
2 distribution by increasing the sample size. The obtained particle data are then filtered and  
3 modified as described in the following section.

## 4 5 2.2 Post-Experimental Data Analysis

6 Both overlapping and foreign particles (such as dust and fibres) are removed from the recorded  
7 particles by utilising the built-in filters of Morphologi G3 software in order to eliminate their  
8 negative effect on particle data before determination of the particle size distributions. Thus,  
9 after running a sensitivity test to find a proper filtering method, particles with both convexity  
10 and solidity lower than 0.85 are excluded from the data obtained from all the experiments.

11 Morphologi G3 captures images of the particles from the planes perpendicular to the axis of  
12 the objective lens and various particle size and shape features are analysed. Since the particles  
13 of interest are acicular, the volume distribution of the particle size, as commonly calculated  
14 using the CE (circle equivalent) diameter with the assumption that the particles are spherical,  
15 cannot be used here. Therefore, the following approach, based on assumptions on the thickness  
16 and orientation of the particles, is adopted. First, it is assumed that all the crystals lie with their  
17 maximum stable plane facing the microscope lens. The second assumption is that all the  
18 particles are rectangular cuboids; the thickness being the dimension hidden from the view. In  
19 the case of  $\beta$  L-glutamic acid and benzothiazin crystals, their thickness is assumed constant,  
20 so the difference in their volumes can be displayed by the difference in their scanned projected  
21 areas. This assumption is justified for  $\beta$  L-glutamic acid by the crystal growth habit as  
22 described by Wang et al. [37]. As observed from the SEM images of Fig. 1 (b), the flat and  
23 plate-like morphology of benzothiazin particles suggests that the variations in crystal  
24 thicknesses are negligible. For potassium phosphate crystals, this assumption is not valid, as  
25 the thickness varies with crystal size. However, with regards to their SEM images, the crystals  
26 used here have the tetragonal form [38] and thus their thickness is equal to their width. As the  
27 projected area and width are measured by the instrument and the shape is approximated to a  
28 cuboid, crystal volumes can be estimated.

29  
30 Another important point to mention is that in view of the model crystals being of cuboid shape,  
31 the ‘square-equivalent side length’ is used as the characteristic particle size, shown in this work  
32 by  $d_{SE}$ . This means that the projected area of a particle is converted to the area of a square, the  
33 side length of which will be used as the characteristic size of the particle. This is of course in

1 addition to the use of the crystal length, width and aspect ratio, which have also been  
 2 characterised and used in the analysis. The size distributions of the test particles are determined  
 3 based on the above-mentioned discussions and by the method described in the following  
 4 section. It should be noted that for  $\beta$  L-glutamic acid and benzothiazin crystals, the  
 5 distributions are represented as area percentage distributions, which in turn describe the volume  
 6 distributions.

7

### 8 2.3 Histograms of Particle Size (Area and Volume Percentage Distribution)

9 For  $\beta$  L-glutamic acid and benzothiazin crystals, bins of particle sizes (represented by  $d_i$  in this  
 10 section) are determined with each bin having a size of  $\Delta d_i$ . It should be noted that here,  $d_i$  can  
 11 represent either of the characteristic size, length, width or aspect ratio of the particles. Particles  
 12 are sorted into each size bin by their size, with each bin containing the sum of the projected  
 13 areas corresponding to the particles inside it ( $A_i$ ). A histogram of  $(A_i/A_{tot}) \times 100$  versus  $d_i$ ,  
 14 where  $A_{tot}$  is the sum of the projected area of all the particles, is used to represent the size  
 15 distribution.

16

$$F_{A,i} = \frac{A_i}{A_{tot}} \times 100 \quad \sum F_{A,i} = 100 \quad (1)$$

17

$$A_{tot} = \sum A_i \quad (2)$$

18

$$\Delta d_i = d_i - d_{i-1} \quad i = 1, d_0 = 0 \quad (3)$$

19

20 The same approach is used for potassium phosphate crystals by using particle volume instead  
 21 of projected area, volume being the product of particle width and projected area ( $V_i = W_i \times A_i$ ).  
 22 The distributions are presented in continuous form by smoothening over 11 points using a  
 23 moving average in order to accurately represent the actual curve without causing any change  
 24 in the trend.

25

## 26 3. Experimental Results and Discussion

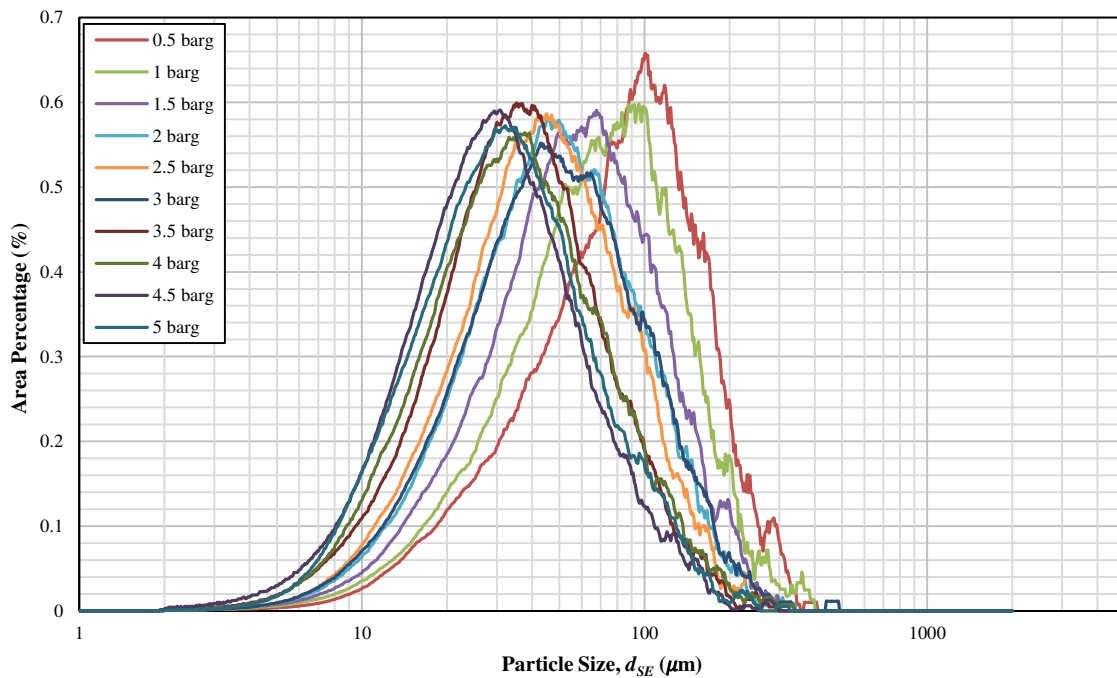
27

### 3.1 Change in Particle Size Distribution

Area percentage distributions of  $\beta$  L-glutamic acid and benzothiazin crystals, and volume percentage distributions of potassium phosphate particles as a function of particle size (square-equivalent side length) after dispersion by Morphologi G3 are displayed in Figs 2, 3 and 4, respectively. Characteristic measures  $D_{10}$ ,  $D_{50}$  and  $D_{90}$  of the square-equivalent side length distributions by volume/area after dispersion are given in Table A1 and Fig. A10 to A12 of Appendix A. Observations by microscopy indicate that crystals dispersed at the lowest pressure of 0.5 barg do not undergo notable breakage. Hence, in this analysis they are assumed as ‘unbroken’ and considered as the reference feed particles for calculating the shift in particle size distribution at larger dispersion pressures. It should also be noted that fluctuations in the curves at certain sizes show that there are not enough particles of such sizes in the distribution to yield a smooth curve. This can be fixed by increasing the amount of the samples through running more experiments.

For  $\beta$  L-glutamic acid and benzothiazin, there is a general shift of the particle size distributions to the left of the plot with increase in the magnitude of the dispersion pressure pulse considering Figs 2 and 3. This indicates that there is a general reduction in the size of the particles as the pressure by which they are dispersed, is increased. This is also evident considering the characteristic measures of the square-equivalent side length  $D_{10}$ ,  $D_{50}$  and  $D_{90}$ , represented in Figs. A10 and A11, Appendix A. As observed in Figs 2 and 3, large particles gradually ‘disappear’ from the distribution, while small particles emerge in the distribution as the dispersion pressure is increased. Additionally, modes of the distributions move to the left as the pressure is increased. However, such trends do not completely follow when the curves are compared for some consecutive pressures, e.g. 2.5 barg with 3 barg for  $\beta$  L-glutamic acid and benzothiazin. This might be attributed to the change in impact velocities at high pressure pulses being less notable. These observations are also confirmed by the changes in the characteristic measures of the square-equivalent side length  $D_{10}$ ,  $D_{50}$  and  $D_{90}$  for each experiment. Comparison of the reference distribution curve (0.5 barg) with each of the other curves for  $\beta$  L-glutamic acid and benzothiazin crystals shows that the higher the dispersion pressure, these changes in particle size become more notable.

1



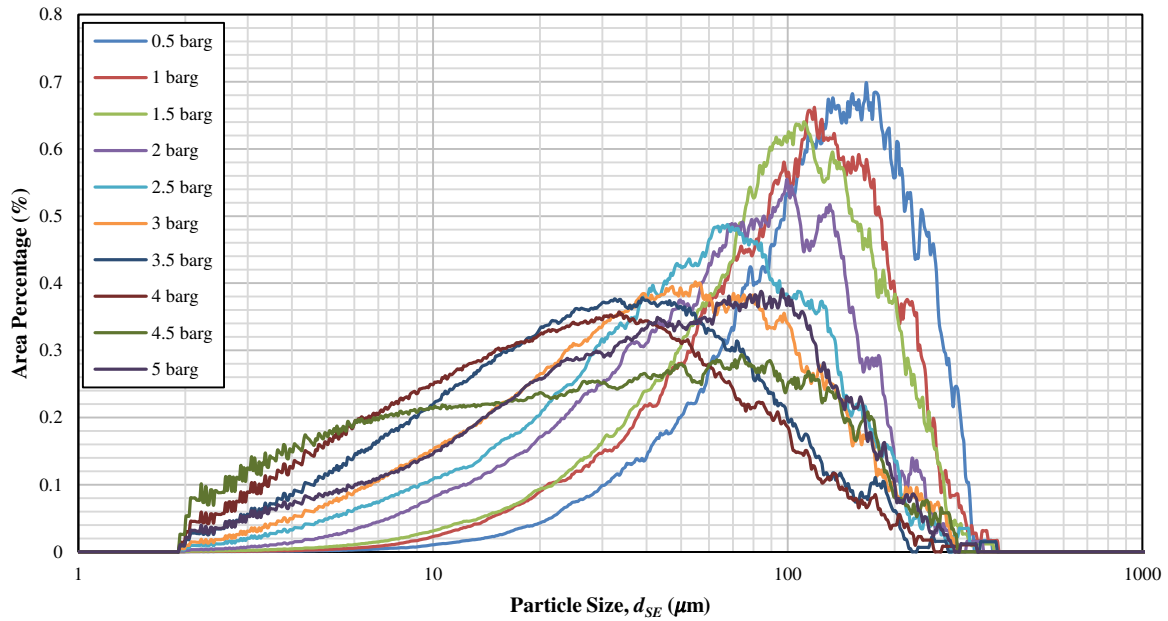
2

3 Fig. 2. Area percentage distribution of  $\beta$  L-glutamic acid crystals dispersed by 0.5, 1, 1.5, 2, 2.5, 3, 3.5, 4, 4.5 and 5 barg  
4 pressures.

5

6 Considering Figs A10 and A11 of Appendix A, and the size distribution curves with regards to  
7  $\beta$  L-glutamic acid and benzothiazin particles represented respectively in Figs 2 and 3, particle  
8 size generally decreases with increase in dispersion pressure. For  $\beta$  L-glutamic acid crystals,  
9 this trend is rapid up to the dispersion pressure of 2.5 barg, then slows down with any further  
10 increase in pressure. However, such trend follows at an almost constant rate for benzothiazin  
11 crystals up to the dispersion pressure of 4 barg. Nevertheless, 4.5 and 5 barg data points deviate  
12 from the trend line.

1

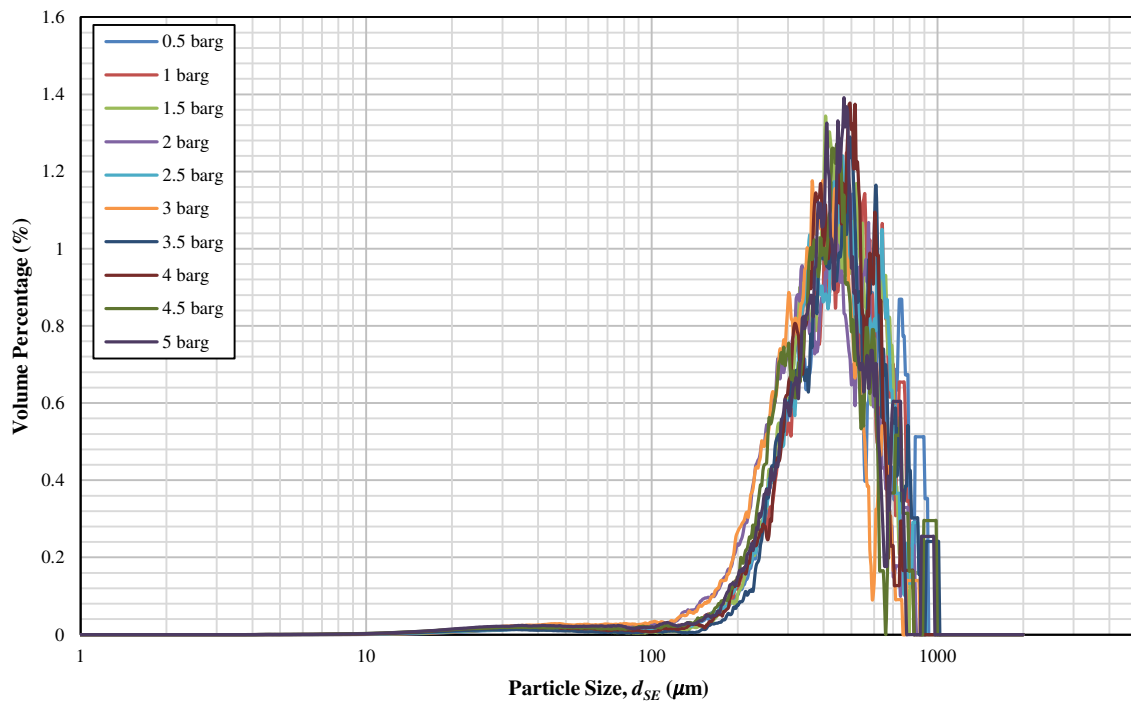


2

3 Fig. 3. Area percentage distribution of benzothiazin crystals dispersed by 0.5, 1, 1.5, 2, 2.5, 3, 3.5, 4, 4.5 and 5 barg  
4 pressures.

5

6 Considering Fig. 4, the fluctuations in the distribution curves of potassium phosphate crystals  
7 are more significant compared to those of  $\beta$  L-glutamic acid and benzothiazin crystals. As  
8 mentioned before, this is due to the low particle count per sample for these particles (around  
9 tens of thousands of particles were analysed for each experiment). Moreover, as suggested by  
10 the CFD results discussed later below, the relatively larger size and higher density of potassium  
11 phosphate crystals do not allow them to collide with the walls of the dispersion spool at high  
12 impact velocities. The shift in the size distribution of potassium phosphate crystals is shown in  
13 Fig. 4. Unlike the other two test materials, there is no substantial shift to the left in the modes  
14 of the curves and the changes are notably small. This shows that the pressure pulses exerted by  
15 Morphologi G3 are not sufficiently strong to cause fragmentation and size reduction is thus  
16 mainly through chipping from the edges and corners of the crystals.



2

3 Fig. 4. Volume percentage distribution of potassium phosphate crystals dispersed by 0.5, 1, 1.5, 2, 2.5, 3, 3.5, 4, 4.5 and 5  
4 barg pressures.

5

### 6 3.2 Change in Length, Width and Aspect Ratio Distributions

7 As the crystals are acicular, the changes in their length, width and aspect ratio are also analysed  
8 to determine how they break. Percentage distributions by volume/area of particles length, width  
9 and aspect ratio along with their characteristic percentile measures are reported in Appendix  
10 A, Figs A1 to A9 and A13 to A21, and Table A2 to A4. With regards to Figs A1 and A2,  
11 Appendix A, there is a significant decrease in the length of  $\beta$  L-glutamic acid and benzothiazin  
12 crystals as the dispersion pressure is increased, indicative of the crystals breaking perpendicular  
13 to their length. Considering Table A2 and Fig. A14, Appendix A, the trend of decrease in length  
14 with pressure is steady for benzothiazin crystals up to the dispersion pressure of 4 barg.  
15 However, the 4.5 and 5 barg dispersion pressures do not seem to decrease the crystal length as  
16 effectively as the first seven dispersion pressures. As for  $\beta$  L-glutamic acid crystals, Fig. A13,  
17 Appendix A, suggests that the trend is rapid up to the dispersion pressure of 2.5 barg. It then  
18 slows down as the pressure is further increased. In contrast to  $\beta$  L-glutamic acid and  
19 benzothiazin crystals, potassium phosphate crystals show a slight yet negligible reduction in  
20 length as the dispersion pressure is increased, suggesting the crystals do not experience

1 noticeable breakage perpendicular to their lengths and undergo chipping rather than  
2 fragmentation (see Figs A3 and A15, Appendix A).

3

4 Considering the characteristic measures of the particle width distribution by volume/area  $W_{10}$ ,  
5  $W_{50}$  and  $W_{90}$  in Table A3, Appendix A,  $\beta$  L-glutamic acid and potassium phosphate crystals  
6 show an insignificant decrease in their widths after dispersion. This suggests that the breakage  
7 does not significantly affect the width of the particles, i.e. the crystals do not break  
8 perpendicular to their width (also see Figs A16 and A18, Appendix A). Interestingly,  
9 considering Table A3 and Fig. A17, Appendix A, benzothiazin crystals display a relatively  
10 noticeable decrease in their widths as the dispersion pressure is increased, suggesting that the  
11 crystals break also perpendicular to their widths. This explains the more notable widening of  
12 the distribution curves for benzothiazin crystals, compared to  $\beta$  L-glutamic acid crystals with  
13 reference to Figs 2 and 3.

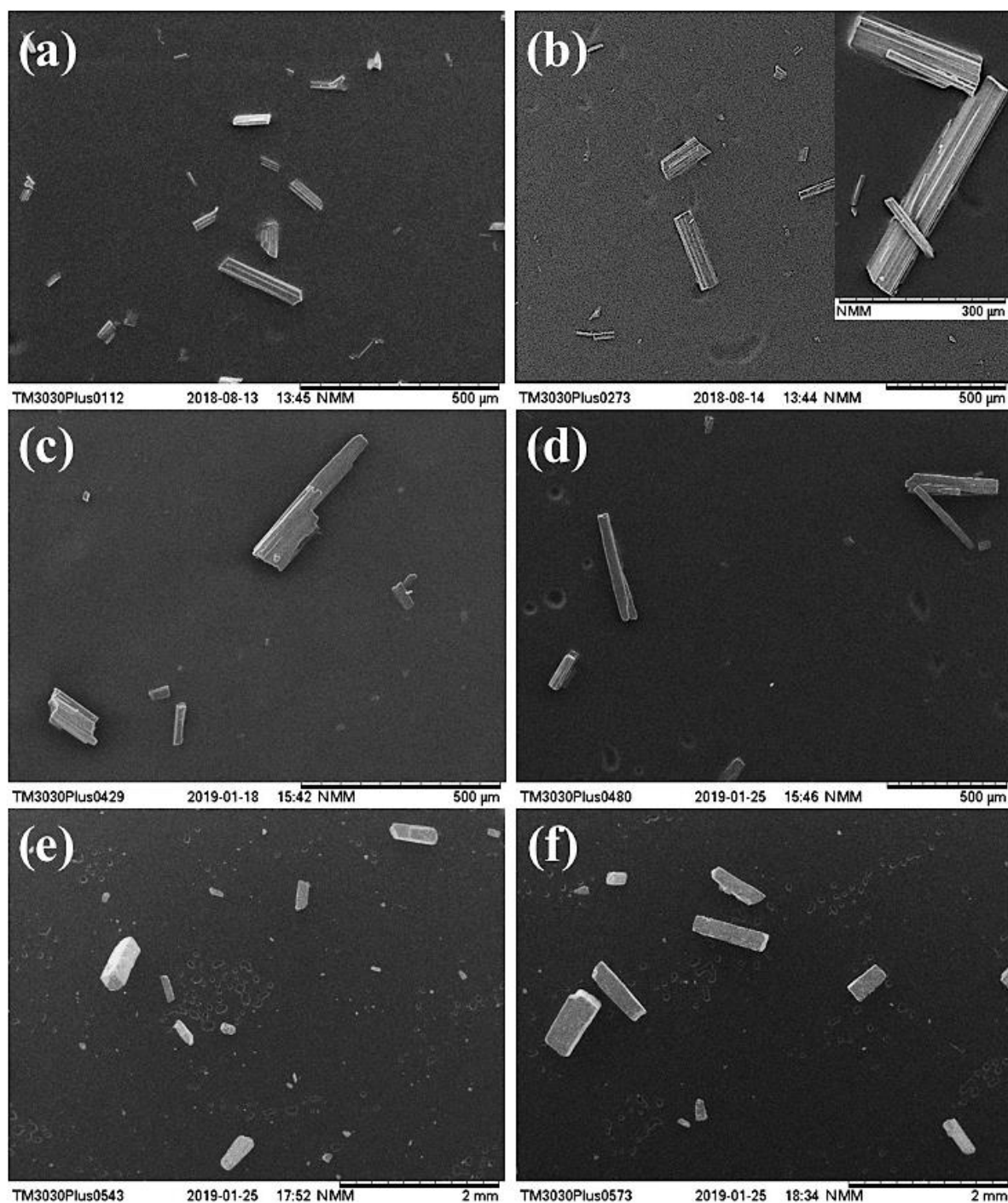
14

15 Characteristic measures of the particle aspect ratio (width to length) distribution by  
16 volume/area  $AR_{10}$ ,  $AR_{50}$  and  $AR_{90}$  are given in Table A4, Appendix A. With regards to the data  
17 corresponding to  $\beta$  L-glutamic acid crystals and Fig. A19, Appendix A, the particle aspect  
18 ratios considerably increase with the increase in dispersion pressure. This is in accordance with  
19 the previous observations regarding the change in the length and width of the said crystals after  
20 dispersion. As for benzothiazin crystals, considering Table A4 and Fig. A20, Appendix A, a  
21 moderate increase in the aspect ratios of the crystals is observed as the dispersion pressure is  
22 increased. Hence, considering the previous conclusion that both width and length of  
23 benzothiazin crystals decrease during dispersion, the decrease in crystal length is relatively  
24 more extensive than that in crystal widths. The negligible change in the aspect ratio of  
25 potassium phosphate crystals is in line with the observation that neither the length nor width  
26 of the crystals changes significantly due to dispersion (see Fig. A21, Appendix A).

27

28 Scanning electron micrographs of the crystals taken after dispersion by 3 and 5 barg pressure  
29 pulses along with optical microscope images of the crystals lying on the glass slide after being  
30 dispersed by 0.5, 1, 2, 3, 4 and 5 barg pressure pulses, respectively shown in Figs 5 and 6, also  
31 confirm the aforementioned observations.

32



1  
 2 Fig. 5. Scanning electron microscopy (SEM) images of:  $\beta$  L-glutamic acid crystals after dispersion by 3 barg (a) and 5 barg  
 3 (b) pressure pulses; benzothiazin crystals after dispersion by 3 barg (c) and 5 barg (d) pressure pulses; potassium phosphate  
 4 crystals after dispersion by 3 barg (e) and 5 barg (f) pressure pulses.

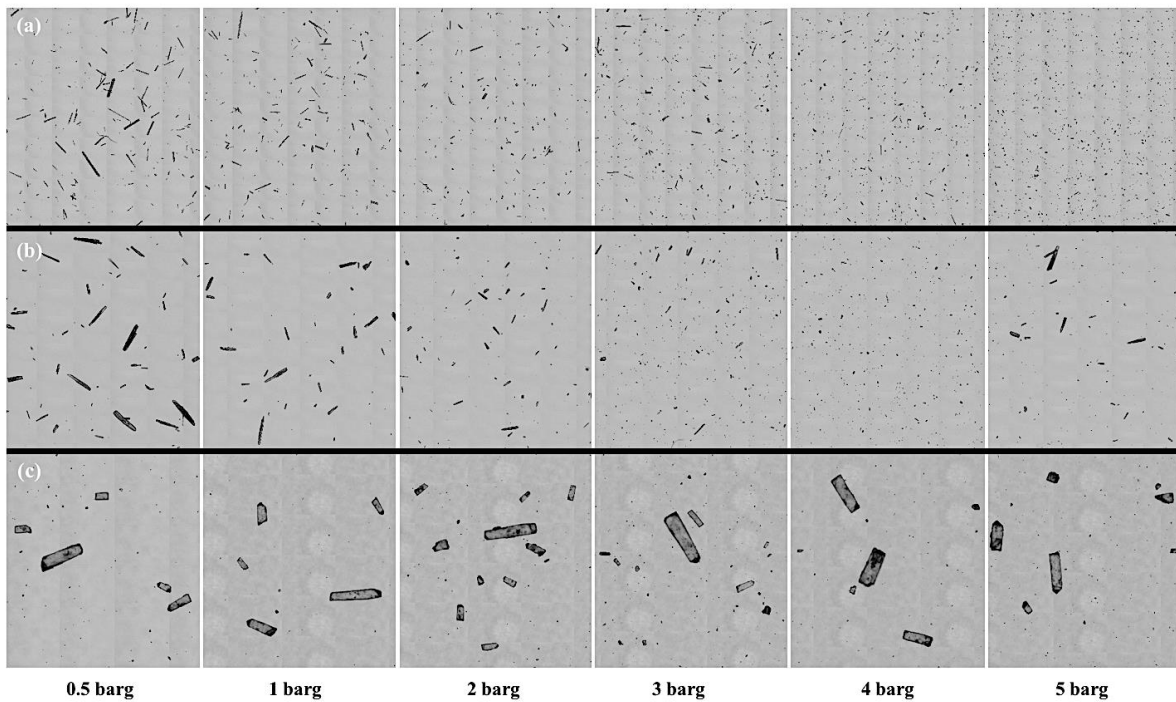
5  
 6 With regards to Figs 5 and 6, the long acicular crystals of  $\beta$  L-glutamic acid and benzothiazin  
 7 have broken into short fragments and chips, whereas potassium phosphate crystals do not seem  
 8 to have undergone a significant change other than a slight increase in the number of chips.

1 Considering Fig. 5 (b), surfaces of  $\beta$  L-glutamic acid crystals do not appear to be smooth as  
2 there are stripes along the crystal length on the surfaces. These might be perceived as surface  
3 defects which seem to chip away from the crystals as they are dispersed. The minute decrease  
4 in the widths of  $\beta$  L-glutamic acid crystals, as observed previously, may be attributed to the  
5 detachment of these thin platelets. The images represented in Figs 5 and 6, along with the  
6 previous observations on the length and width of the crystals suggest that  $\beta$  L-glutamic acid  
7 crystals preferentially break perpendicular to their lengths. Obviously, the bending moment  
8 perpendicular to the crystal length is accountable for the tensile stress, but the potential  
9 presence of cleavage planes along the width of the crystals could facilitate the process.

10

11 Benzothiazin crystals break perpendicular to both their length and width. An interesting  
12 observation is that not many chips form, and mostly fragments are generated when the crystals  
13 are dispersed by the 5 barg pressures as compared to when dispersed by the 3 barg pressure.  
14 This supports the observations from Figs A11, A14, A17 and A20, Appendix A, with regards  
15 to the deviation of 5 barg data points from the general trend, which suggests that the 5 barg  
16 dispersion pressure pulse does not break benzothiazin crystals much further than the 3 barg  
17 pressure pulse does. The difference in breakage patterns of  $\beta$  L-glutamic acid and benzothiazin  
18 crystals shows that aside from the feed particle size and impact velocity, the crystal structure  
19 plays an important role in the pattern of breakage. The breakage perpendicular to the length of  
20 benzothiazin crystals could have been initiated by the same mechanism as of  $\beta$  L-glutamic acid  
21 crystals. However, the breakage perpendicular to the width of benzothiazin crystals is  
22 potentially due to the presence of cleavage planes along that direction as the bending moment  
23 acting perpendicular to the width is not significant compared to that acting perpendicular to the  
24 length. These observations suggest that the disperser of Morphologi G3 is a suitable device for  
25 evaluation of particle impact breakage. However, for strong particles such as potassium  
26 phosphate, the test may only reveal the chipping propensity.

1



2

3 Fig. 6. Composite images of the crystals after dispersion by 0.5, 1, 2, 3, 4 and 5 barg pressure pulses for:  $\beta$  L-glutamic acid  
4 crystals (a); benzothiazin crystals (b); potassium phosphate crystals (c).

5

### 6 3.3 Analysis of Breakage

7 In the disperser of Morphologi G3, particle impact velocity is a function of the dispersion  
8 pressure pulse. Thus, information on the extent of breakage as a function of the magnitude of  
9 the dispersion pressure pulse is required in order to analyse particle breakage. The extent of  
10 breakage,  $R^*$ , as given by Eq. (4), is a gravimetric ratio of the mass of the daughter particles to  
11 the mass of the feed particles, expressed in percentage.

12

$$13 \quad R^* = \frac{M_d}{M_f} \times 100 \quad (4)$$

14

15 where  $M_d$  and  $M_f$  represent the mass of daughter and feed particles, respectively. However,  
16 optical microscopy does not provide gravimetric information. Nevertheless, distributions based  
17 on the projected area/volume of the particles can be obtained as shown previously. Thus,  
18 assuming that all the particles are rectangular cuboids and that the density does not change  
19 during breakage, the gravimetric ratio is equivalent to volume ratio and consequently related  
to area and thickness ratio as given by:

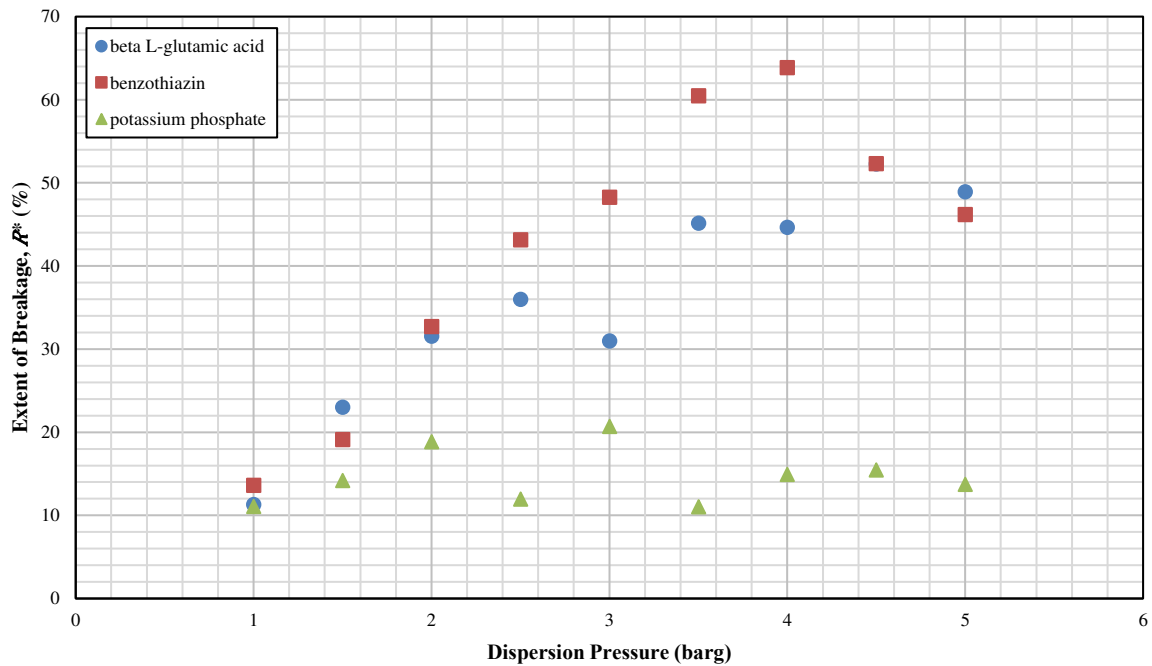
1

$$R^* = \frac{M_d}{M_f} = \frac{V_d}{V_f} = \frac{A_d \times h_d}{A_f \times h_f} \quad (5)$$

2

3 where  $V_d, A_d$  and  $h_d$  represent the volume, projected area and thickness of the daughter particles,  
4 respectively and  $V_f, A_f$  and  $h_f$  represent those of the feed particles. With regards to Eq. (5) and  
5 based on the assumption of  $\beta$  L-glutamic acid and benzothiazin crystals having constant  
6 thicknesses ( $h_d = h_f$ ), the area percentage distributions can be used to obtain  $R^*$ . In the case of  
7 potassium phosphate crystals, volume percentage distributions are used as the thickness is  
8 approximately equal to the width and thus  $V_d/V_f = (A_d \times W_d/A_f \times W_f)$ ;  $W_d$  and  $W_f$  being the width  
9 of the daughter and mother particles, respectively. The percentage distributions are first  
10 converted to probability density distributions. Consequently, the extent of breakage can be  
11 determined by comparing the size distribution curve of the particles dispersed at each  
12 dispersion pressure to that of the particles dispersed at 0.5 barg (taken as the reference  
13 distribution, i.e. assuming little/no crystal breakage at this pressure pulse). The area of positive  
14 difference (in percentage) between the probability density distribution curve of the reference  
15 particles and that of the data of interest, when subtracting the former from the latter, can  
16 represent the  $R^*$  caused by the corresponding dispersion pressure. The extent of breakage as a  
17 function of dispersion pressure for  $\beta$  L-glutamic acid, benzothiazin and potassium phosphate  
18 crystals is thus calculated and represented in Fig. 7. As it can be observed, the extent of  
19 breakage increases with the dispersion pressure for  $\beta$  L-glutamic acid and benzothiazin  
20 crystals. The rise is fast with a similar slope and close values for both test materials up to the  
21 pressure of 2 barg. However, it slows down with further increase in pressure for  $\beta$  L-glutamic  
22 acid crystals, while it continues with the same rate up to the pressure of 4 barg for benzothiazin  
23 crystals, following which it surprisingly decreases.

1



2

3 Fig. 7. Extent of breakage of  $\beta$  L-glutamic acid, benzothiazin and potassium phosphate crystals as a function of dispersion  
4 pressure using the 0.5 barg distribution as reference.

5

6 With regards to potassium phosphate crystals, the extent of breakage does not increase with  
7 increase in dispersion pressure except for the first three pressures. There is a significant scatter  
8 in the data points with no clear trend. As discussed before, this is due to the fact that the crystals  
9 undergo chipping. However, since the number of the produced chips is insufficient to produce  
10 reliable results, the breakage of these crystals is not further analysed. A modification of the  
11 spool design is needed to induce higher impact velocities for such large crystals in order to  
12 cause their breakage.

13

14 Ghadiri and Zhang [21] model is used to analyse the breakage of the crystals, Eq. (6).

15

$$R^* = \alpha \frac{H}{K_c^2} \rho D V^2 = \psi \rho D V^2 \quad (6)$$

16

17 where  $\alpha$  is a proportionality constant and  $\rho$  is the density of the particle.  $D$  denotes a linear  
18 dimension of the particle, whereas  $V$ ,  $H$  and  $K_c$  represent the impact velocity, the hardness and  
19 the fracture toughness of the particles, respectively.  $\psi$  ( $\alpha H/K_c^2$ ) is a lumped parameter

1 describing the mechanical properties of the particle that are responsible for plastic deformation  
2 and fracture toughness, known as the *breakability index* [25]. This parameter reflects the ease  
3 with which the particle breaks. Considering Eq. (6), if  $R^*$  is plotted as a function of  $\rho DV^2$ , a  
4 unification of data is expected with the slope of the line indicating  $\psi$ . In order to find the impact  
5 velocity of the feed particles dispersed at different pressures, CFD calculations are carried out  
6 as described below.

## 8 4. CFD Modelling

### 10 4.1 Computational Details and Numerical Solution Method

11 Three-dimensional Computational Fluid Dynamics (CFD) modelling method is used with  
12 transient, compressible flow assumption to predict gas velocity profiles in the disperser.  
13 Turbulence modelling is carried out using scale adaptive simulation method [39]. The  
14 continuous and discrete phase equations are solved using commercial CFD software Ansys  
15 Fluent (2018). The time step for particles tracking and for the continuous phase is set at  $5.0 \times 10^{-6}$   
16 s. The simulation is run at the specified inlet pressure for 20 ms; thereafter the pulse is stopped  
17 by changing the pressure to 0 barg. Details of the CFD modelling methodology and the mesh  
18 used in the CFD simulations can be found in a recent work carried out by Ali and Ghadiri [40]  
19 in which they studied triboelectric charging of particles in G3 disperser using CFD modelling.

### 21 4.2 Modelling of Particle Trajectories

22 The discrete phase is considered to comprise rectangular cuboid particles with the dimensions  
23 given in Table 1. The density of crystals is considered to be constant with a value of 1600  
24  $\text{kg/m}^3$  for  $\beta$  L-glutamic acid, 1197  $\text{kg/m}^3$  for benzothiazin and 2340  $\text{kg/m}^3$  for potassium  
25 phosphate. The particles are initially placed in the sample well and get dispersed due to a pulse  
26 of pressurised air. The trajectories of particles are computed by solving the equation of motion  
27 of particles considering the drag and gravitational forces. For these particle shapes, the drag  
28 coefficient is calculated using correlations given by Ganser [41]. The rotation of particles is  
29 not considered. One-way coupling is assumed between the particles and the air, i.e. the air flow  
30 influences the trajectories of particles, but the momentum exerted by the particles on the air is  
31 ignored. The interaction between the particles, i.e. particle-particle collisions is also not  
32 considered. In a previous study by Ali and Ghadiri [40], it was found that the maximum impact  
33 velocity of particles in the disperser took place at the wall just above the sample well (a

1 schematic of the Morphologi G3 dispersion spool is attached in Appendix B, Fig. B1). For the  
 2 purpose of predicting the impact velocity, the velocity of particles colliding with the walls in  
 3 this region is recorded and the impacted particles are eliminated from the computational  
 4 domain. To get a statistically representative impact velocity, 1000 particles are tracked for each  
 5 size. For each case, the simulation is continued until all the particles exit the domain.

6

7 Table 1. Dimensions of model test crystals considered in the study.

<b><math>\beta</math> L-glutamic acid</b>			<b>benzothiazin</b>			<b>potassium phosphate</b>		
<b>Length</b>	<b>Width</b>	<b>Thickness</b>	<b>Length</b>	<b>Width</b>	<b>Thickness</b>	<b>Length</b>	<b>Width</b>	<b>Thickness</b>
<b>(<math>\mu\text{m}</math>)</b>	<b>(<math>\mu\text{m}</math>)</b>	<b>(<math>\mu\text{m}</math>)</b>	<b>(<math>\mu\text{m}</math>)</b>	<b>(<math>\mu\text{m}</math>)</b>	<b>(<math>\mu\text{m}</math>)</b>	<b>(<math>\mu\text{m}</math>)</b>	<b>(<math>\mu\text{m}</math>)</b>	<b>(<math>\mu\text{m}</math>)</b>
1000	50	20	1000	60	20	2000	270	180
500	50	20	500	60	20	1000	270	180
250	50	20	250	60	20	500	270	180
50	50	20	60	60	20	270	270	180

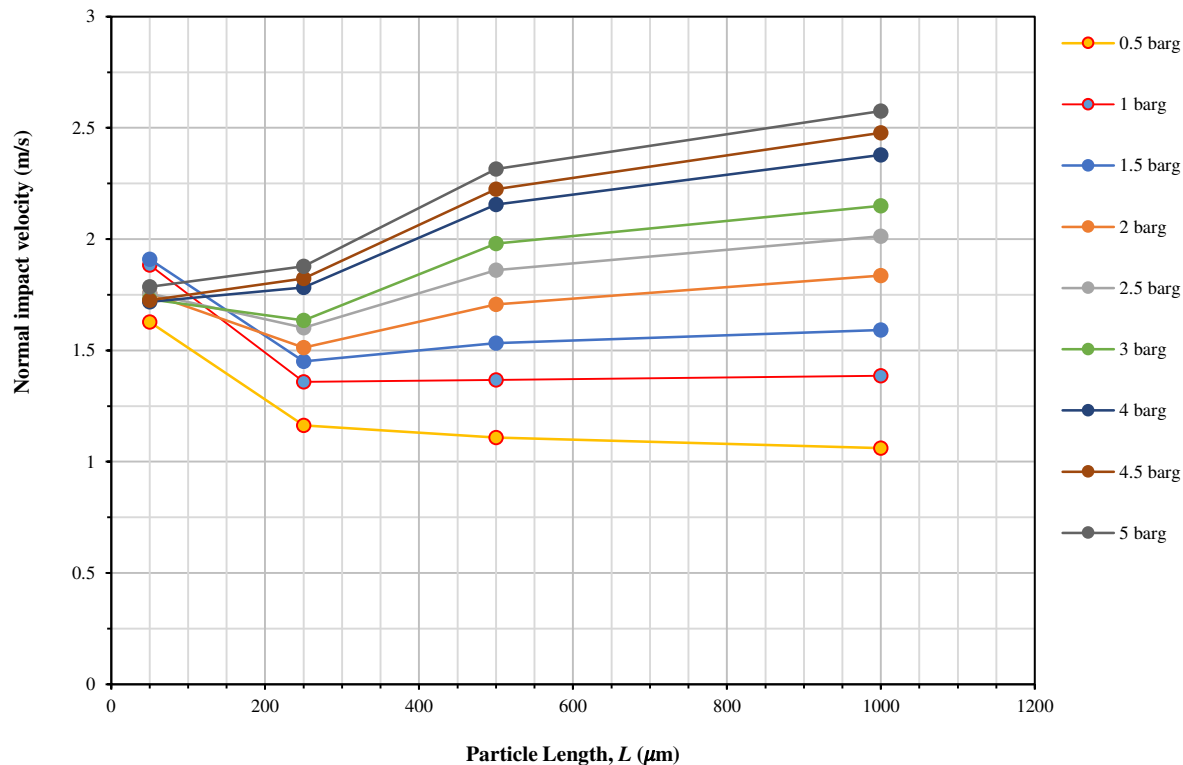
8

9

### 10 4.3 CFD Modelling Results

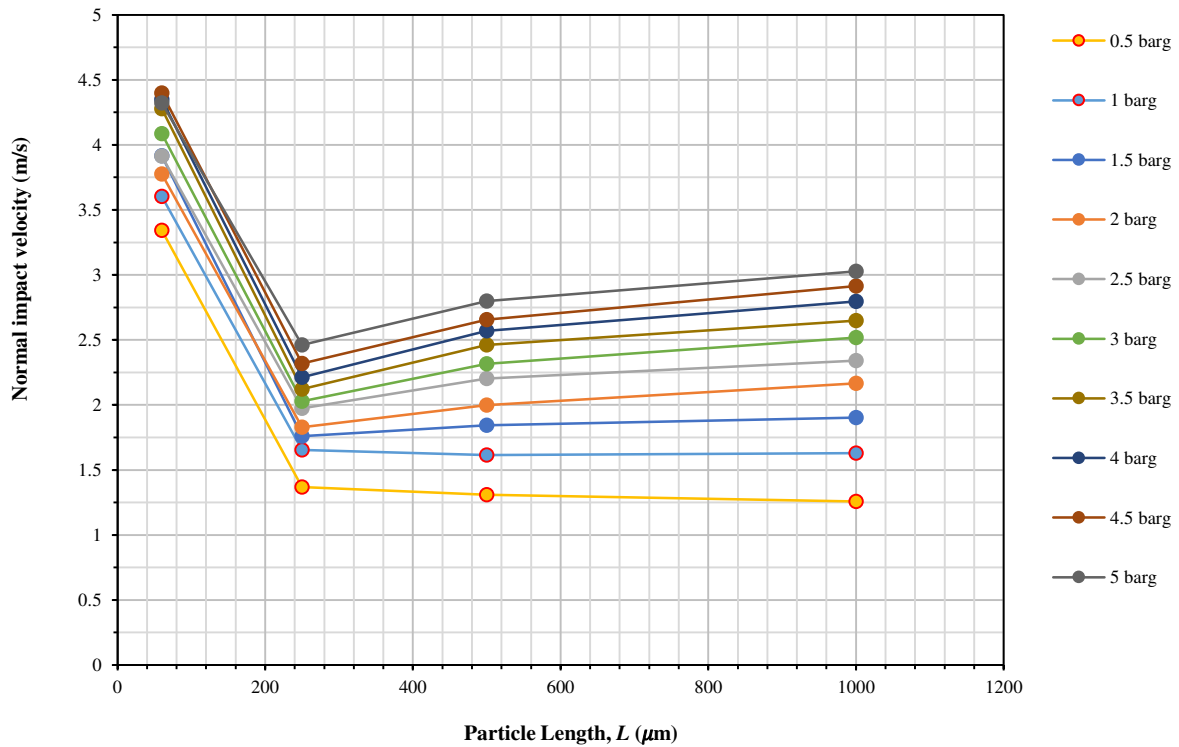
11 The study of the influence of inlet air pressure on the impact velocity of particles is carried out  
 12 by using different inlet air pressure pulses. The simulation runs were carried out at 0.5, 1.0,  
 13 1.5, 2.0, 2.5, 3.0, 3.5, 4.0, 4.5 and 5.0 barg inlet air pressure pulses. A plot of cross-sectional  
 14 view of the contour plots of air velocity coloured by velocity magnitude for selected inlet air  
 15 pressure pulses can be found in Appendix B, Fig. B2. An increase in the air velocity near the  
 16 tip of the inlet nozzle is predicted with increasing the inlet air pressure. After the 1 barg  
 17 pressure, the maximum velocity just at the exit of the inlet nozzle exceeds the sonic velocity.

18 The average normal and total impact velocities (normal and tangential components) of  $\beta$  L-  
 19 glutamic acid crystals impacting on the wall just above the sample well are depicted in Fig. 8  
 20 and Appendix B, Fig. B3, respectively. The normal component as well as the total impact  
 21 velocity are strongly affected by the dispersion pressure pulse. The effect of particle length on  
 22 impact velocity is more complicated, as it is generally pronounced for particle lengths smaller  
 23 than 250  $\mu\text{m}$ , but largely invariant for larger particles.



1  
 2 Fig. 8. Average normal impact velocity of  $\beta$  L-glutamic acid crystals of different sizes at different inlet air pressures.

3  
 4 The distribution of impact velocities of  $\beta$  L-glutamic acid crystals of different sizes at 0.5 and  
 5 5 barg pressures is depicted in Appendix B, Fig. B4. For a given particle size, a range of particle  
 6 impact velocities is predicted, this is due to the transient nature of the operation of the disperser.  
 7 As the high velocity air stream exiting from the inlet nozzle starts to impinge on the sample  
 8 well, the particles start to accelerate towards the wall and collide with it. The smallest particle  
 9 size exhibits the largest variation in the impact velocities at both 0.5 and 5 barg inlet air  
 10 pressures, while the largest particles have the narrowest distribution. Qualitatively, the trend of  
 11 distribution of impact velocities for both 0.5 and 5 barg cases for each size is similar.



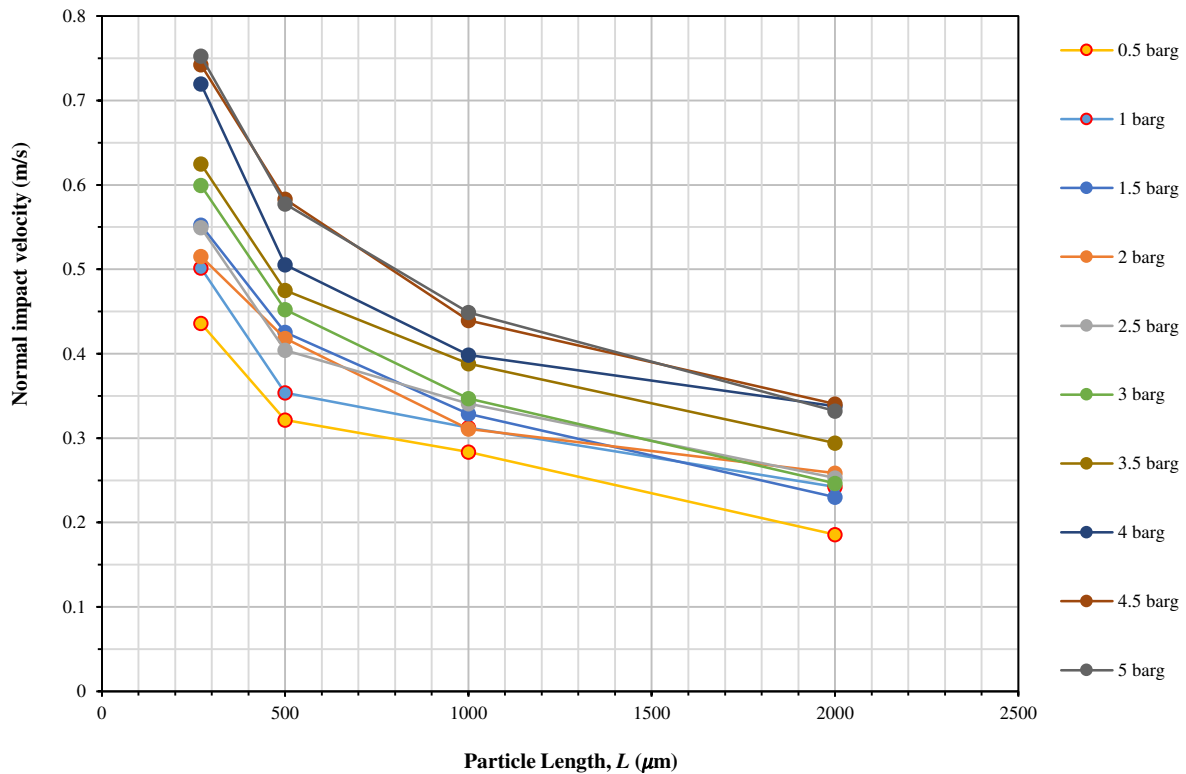
2

3 Fig. 9. Average normal impact velocity of benzothiazin crystals of different sizes at different inlet air pressures.

4

5 The average normal and total impact velocities of benzothiazin crystals impacting on the wall  
6 just above the sample well are depicted in Fig. 9 and Appendix B, Fig. B5, respectively. The  
7 size distribution of benzothiazin crystals is similar to that of  $\beta$  L-glutamic acid crystals, but  
8 their density is lower. As a result, benzothiazin crystals have higher normal and total impact  
9 velocities compared to  $\beta$  L-glutamic acid crystals. The distribution of impact velocities of  
10 benzothiazin crystals is given in Appendix B, Fig. B6 as a frequency distribution. The particles  
11 with the smallest length have the highest velocities for both 0.5 and 5 barg pressures; a trend  
12 similar to that predicted for  $\beta$  L-glutamic acid crystals.

1



2

3 Fig. 10. Average normal impact velocity of potassium phosphate crystals of different sizes at different inlet air pressures.

4

5 The average normal and total impact velocity of potassium phosphate crystals impacting on  
6 the wall above the sample well is depicted in Fig. 10 and Appendix B, Fig. B7. These crystals  
7 have a wider size distribution and higher density compared to  $\beta$  L-glutamic acid and  
8 benzothiazin crystals. As a result, the predicted velocities in this case for all the pressures are  
9 significantly lower. The frequency distribution of impact velocities is also relatively narrow as  
10 depicted in Appendix B, Fig. B8. Finally, the simulation results suggest that most of potassium  
11 phosphate crystals remain inside the sample well within the 20 ms pressure pulse and less than  
12 half of the crystals hit the walls of the dispersion spool. This might be attributed to the large  
13 size and higher density of the crystals.

14

## 15 5. Breakage Propensity

16 Impact velocity is a function of the feed particle size (the length for acicular particles) and  
17 dispersion pressure, as shown in the previous section. Bonakdar et al. [25] used narrow sieve  
18 cuts for the experiments to reduce the spread in the results and thus the same narrow size  
19 distribution was used for CFD calculations [26]. However, the problem with acicular particles

1 is the impracticality of sieving for classifying them into narrow sizes; crystals may align  
 2 perpendicular to the sieve aperture and pass through it, resulting in an inaccurate size  
 3 measurement. Thus, the whole size distribution is used here for acicular particles following the  
 4 method proposed by Goh et al. [42], based on a modification of Ghadiri and Zhang [21]:

$$R^* = \psi \sum_{i=1}^n \rho \phi_i D_i V_i^2 \quad (7)$$

6  
 7 where  $i$  is the bin number,  $\phi$  is the area fraction ( $F_{A,i}/100$ ) of the particles in the bin,  $D$  is the  
 8 upper size limit of the bin and  $V$  is the impact velocity of the particles in the bin. The crystals  
 9 of size  $d_{SE}$  are sorted into bins of size  $D_i$  in order to account for the contribution of each bin to  
 10 the extent of breakage as given by Eq. (7).

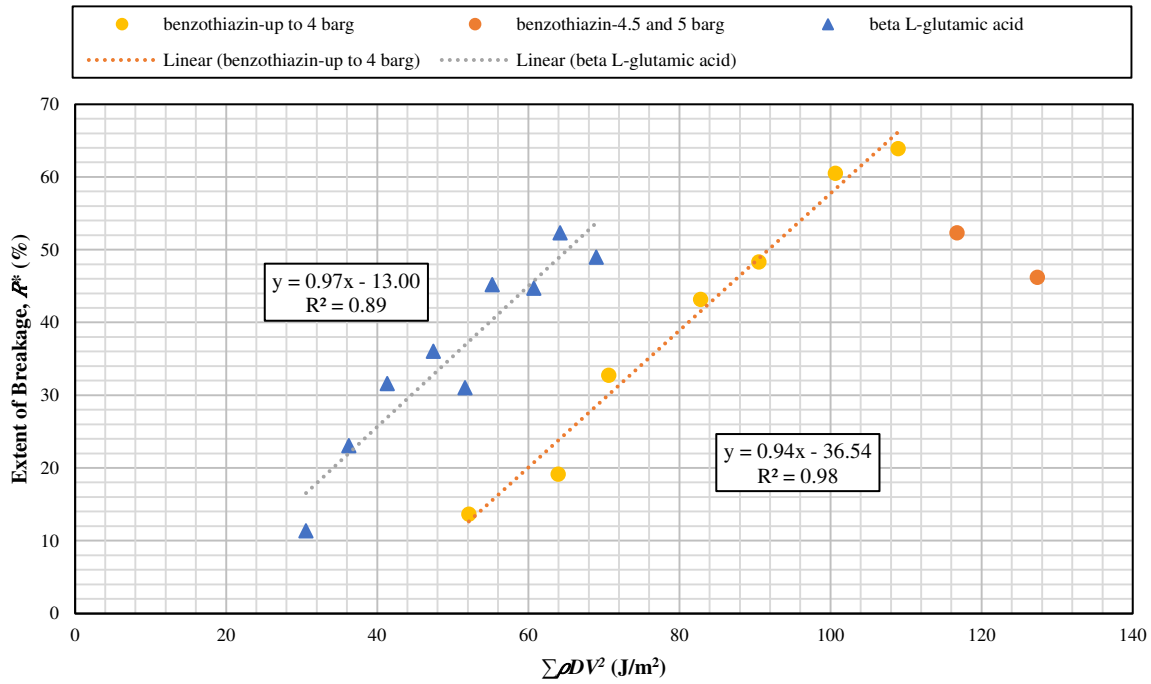
11  
 12 In order to calculate the impact velocity, a relationship needs to be established between the  
 13 characteristic particle size ( $d_{SE}$ ) and the particle length. Since the particle length increases with  
 14 the increase in the characteristic particle size (see Figs A22 and A23, Appendix A), a linear  
 15 relationship is assumed here for these measures of size, as shown by Eq. (8).

$$L = k d_{SE} \quad (8)$$

16  
 17  
 18 where  $L$  is the particle length,  $d_{SE}$  is the characteristic particle size and  $k$  is a constant. In order  
 19 to find  $k$ , the characteristic size,  $d_{SE}$  (square-equivalent side length) is plotted against the length  
 20 corresponding to each particle and the slope of the plot,  $k$ , is then used to find the length  
 21 corresponding to each bin, which in turn is utilised to determine the impact velocity  
 22 corresponding to each bin. Using the obtained values for impact velocity, along with the  
 23 corresponding values for area fraction and particle size,  $\rho \phi_i D_i V_i^2$  is calculated for each bin and  
 24 the resulting values are added.  $\psi$  is then determined as the slope of  $R^*$  versus  $\sum_{i=1}^n \rho \phi_i D_i V_i^2$   
 25 plot. The values of  $k$  are determined as 3.1 and 2.4 for  $\beta$  L-glutamic acid and benzothiazin  
 26 crystals, respectively. The graphs are given in Appendix A, Fig. A22 and Fig. A23. The length  
 27 corresponding to each bin is used to obtain the impact velocity for each bin from the graphs of  
 28 normal impact velocity versus particle length attained by CFD calculations. Finally, by  
 29 considering particle density for  $\beta$  L-glutamic acid and benzothiazin crystals, and using the area  
 30 fractions, sizes and impact velocities corresponding to each bin, the plot of  $R^*$  versus

1  $\sum_{i=1}^n \rho \phi_i D_i V_i^2$  is drawn for both test materials using all dispersion pressures, as represented in  
 2 Fig. 11. The slope of the line describes the breakability index.

3



4

5 Fig. 11. Extent of breakage versus  $\sum \rho D V^2$  for  $\beta$  L-glutamic acid and benzothiazin crystals with the breakability index as the  
 6 slope.

7

8 A good unification of data is observed for both  $\beta$  L-glutamic acid and benzothiazin crystals.  
 9 The breakability index of  $\beta$  L-glutamic acid crystals is 0.97. For benzothiazin crystals, the data  
 10 points corresponding to 4.5 and 5 barg are excluded, thus yielding a breakability index of 0.94.  
 11 This suggests that up to the dispersion pressure of 4 barg, benzothiazin crystals have a breakage  
 12 tendency similar to that of  $\beta$  L-glutamic acid crystals; the crystals break due to fragmentation  
 13 and chipping with the fragmentation regime being dominant. The remarkable deviation of the  
 14 4.5 and 5 barg benzothiazin data points from the trend is consistently reproducible but is not  
 15 understood and requires further investigation. These results are also well in accordance with  
 16 the earlier discussed observations from the crystal images represented in Fig. 6 (b).  
 17 Additionally, the trend might be due to the operation of Morphologi G3 at high pressures and  
 18 needs further investigation, although the trend is stable for  $\beta$  L-glutamic acid crystals and for  
 19 carbamazepine crystals as reported by Goh et al. [42].

20

## 1 Conclusions

2 A new method has been developed to quantitatively determine the breakability of acicular  
3 particles. A pressure pulse is used to disperse a small quantity of acicular crystals, as a result  
4 of which the crystals collide with the disperser wall and break. The extent of breakage is  
5 analysed by measuring the shift in particle size distribution. The results show that for both  $\beta$   
6 L-glutamic acid and benzothiazin, the crystals break into a considerable number of fragments  
7 and platelets, with fragmentation governing the breakage regime. Based on the model of  
8 Ghadiri and Zhang [21] together with CFD simulations for calculating particle impact velocity,  
9 a breakability index is characterised. Its derived value for  $\beta$  L-glutamic acid and benzothiazin  
10 crystals suggests that both test materials have a similar breakage tendency when dispersed by  
11 a pressure pulse of up to 4 barg, as indicated by the slope of the fitted line. However, above the  
12 4 barg dispersion pressure, benzothiazin crystals surprisingly break to a lower extent. The exact  
13 cause of this decline is unknown. Potassium phosphate crystals do not accelerate to sufficiently  
14 high impact velocities to get notable damage and merely experience minor chipping. A  
15 modification of the design of the disperser could provide larger impact velocities, thus making  
16 it possible to break such large crystals. Nevertheless, in cases that the sample supply is scarce,  
17 the use of this method becomes valuable, as it requires only a small amount of sample for  
18 impact breakage. Application of image analysis and post-processing and manipulation of the  
19 raw data allow various size and shape analyses to be conducted, facilitating observation of how  
20 particles undergo size reduction.

21

## 22 Acknowledgement

23 The authors would like to thank Dr Paul Kippax, Malvern Panalytical Ltd for providing  
24 information on the design of G3 disperser for CFD calculations.

25

## 26 References

27

- 28 [1] H. Kalman, Particle Breakage and Attrition, KONA Powder Part. J. 18 (2000) 108–120.  
29 doi:10.14356/kona.2000017.
- 30 [2] B. Biscans, Impact attrition in crystallization processes. Analysis of repeated impacts  
31 events of individual crystals, Powder Technol. 143–144 (2004) 264–272.  
32 doi:10.1016/j.powtec.2004.04.025.
- 33 [3] C.R. Bemrose, J. Bridgwater, A review of attrition and attrition test methods, Powder  
34 Technol. 49 (1987) 97–126. doi:10.1016/0032-5910(87)80054-2.
- 35 [4] K.R. Yuregir, M. Ghadiri, R. Clift, Observations on impact attrition of granular solids,

- 1 Powder Technol. 49 (1986) 53–57. doi:10.1016/0032-5910(86)85004-5.
- 2 [5] K.R. Yüregir, M. Ghadiri, R. Clift, Impact Attrition of Sodium Chloride Crystals, Chem.  
3 Eng. Sci. 42 (1987) 843–853. doi:10.1016/0009-2509(87)80043-X.
- 4 [6] A.D. Salman, M. Szabo, I. Angyal, A. Verba, Particle Degradation, Period. Polytech.  
5 Mech. Eng. 32 (1988) 233–251. doi:https://doi.org/N/A.
- 6 [7] A.D. Salman, D.A. Gorham, A. Verba, A study of solid particle failure under normal  
7 and oblique impact, Wear. 186–187 (1995) 92–98. doi:10.1016/0043-1648(95)07140-7.
- 8 [8] J.A.S. Cleaver, M. Ghadiri, N. Rolfe, Impact attrition of sodium carbonate monohydrate  
9 crystals, Powder Technol. 76 (1993) 15–22. doi:10.1016/0032-5910(93)80036-A.
- 10 [9] Z. Ning, R. Boerefijn, M. Ghadiri, C. Thornton, Distinct element simulation of impact  
11 breakage of lactose agglomerates, Adv. Powder Technol. 8 (1997) 15–37.  
12 doi:10.1016/S0921-8831(08)60477-X.
- 13 [10] R. Boerefijn, Z. Ning, M. Ghadiri, Disintegration of weak lactose agglomerates for  
14 inhalation applications, Int. J. Pharm. 172 (1998) 199–209. doi:10.1016/S0378-  
15 5173(98)00207-5.
- 16 [11] J. Subero, M. Ghadiri, Breakage patterns of agglomerates, Powder Technol. 120 (2001)  
17 232–243. doi:10.1016/S0032-5910(01)00276-5.
- 18 [12] A. Samimi, R. Moreno, M. Ghadiri, Analysis of impact damage of agglomerates: Effect  
19 of impact angle, Powder Technol. 143–144 (2004) 97–109.  
20 doi:10.1016/j.powtec.2004.04.027.
- 21 [13] A.D. Salman, J. Fu, D.A. Gorham, M.J. Hounslow, Impact breakage of fertiliser  
22 granules, Powder Technol. 130 (2003) 359–366. doi:10.1016/S0032-5910(02)00237-1.
- 23 [14] S. Antonyuk, M. Khanal, J. Tomas, S. Heinrich, L. Mörl, Impact breakage of spherical  
24 granules: Experimental study and DEM simulation, Chem. Eng. Process. Process  
25 Intensif. 45 (2006) 838–856. doi:10.1016/j.cep.2005.12.005.
- 26 [15] T. Dumas, O. Bonnefoy, P. Grosseau, G. Thomas, S. Nebut, L. Guy, New methods to  
27 analyse fragmentation mechanisms of precipitated silicas, in: 5th Int. Work.  
28 Granulation, Granulation Conference Lausanne, Switzerland, 2011.
- 29 [16] O. Lecoq, N. Chouteau, M. Mebtoul, J.F. Large, P. Guigon, Fragmentation by high  
30 velocity impact on a target: A material grindability test, Powder Technol. 133 (2003)  
31 113–124. doi:10.1016/S0032-5910(03)00085-8.
- 32 [17] Y. Rozenblat, E. Grant, A. Levy, H. Kalman, J. Tomas, Selection and breakage functions  
33 of particles under impact loads, Chem. Eng. Sci. 71 (2012) 56–66.  
34 doi:10.1016/j.ces.2011.12.012.
- 35 [18] O. Lecoq, A. Chamayou, J.A. Dodds, P. Guigon, Application of a simplifying model to  
36 the breakage of different materials in an air jet mill, Int. J. Miner. Process. 112–113  
37 (2012) 7–12. doi:10.1016/j.minpro.2012.04.004.
- 38 [19] L. Vogel, W. Peukert, Breakage behaviour of different materials - Construction of a  
39 mastercurve for the breakage probability, Powder Technol. 129 (2003) 101–110.  
40 doi:10.1016/S0032-5910(02)00217-6.
- 41 [20] R. Weichert, Correlation between probability of breakage and fragment size distribution  
42 of mineral particles, Int. J. Miner. Process. 22 (1988) 1–8. doi:10.1016/0301-

- 1 7516(88)90052-X.
- 2 [21] M. Ghadiri, Z. Zhang, Impact attrition of particulate solids. Part 1: A theoretical model  
3 of chipping, *Chem. Eng. Sci.* 57 (2002) 3659–3669. doi:10.1016/S0009-  
4 2509(02)00240-3.
- 5 [22] A. Samimi, M. Ghadiri, R. Boerefijn, A. Groot, R. Kohlus, Effect of structural  
6 characteristics on impact breakage of agglomerates, *Powder Technol.* 130 (2003) 428–  
7 435. doi:10.1016/S0032-5910(02)00246-2.
- 8 [23] C. Subero-Couroyer, M. Ghadiri, N. Brunard, F. Kolenda, Analysis of catalyst particle  
9 strength by impact testing: The effect of manufacturing process parameters on the  
10 particle strength, *Powder Technol.* 160 (2005) 67–80.  
11 doi:10.1016/J.POWTEC.2005.08.005.
- 12 [24] D. Olusanmi, C. Wang, M. Ghadiri, Y. Ding, K.J. Roberts, Effect of temperature and  
13 humidity on the breakage behaviour of Aspirin and sucrose particles, *Powder Technol.*  
14 201 (2010) 248–252. doi:10.1016/j.powtec.2010.04.003.
- 15 [25] T. Bonakdar, M. Ali, S. Dogbe, M. Ghadiri, A. Tinke, A method for grindability testing  
16 using the Scirocco disperser, *Int. J. Pharm.* 501 (2016) 65–74.  
17 doi:10.1016/j.ijpharm.2016.01.052.
- 18 [26] M. Ali, T. Bonakdar, M. Ghadiri, A. Tinke, Particle Breakage in a Scirocco Disperser,  
19 *Powder Technol.* 285 (2015) 138–145. doi:10.1016/j.powtec.2015.06.048.
- 20 [27] T. Bonakdar, M. Ghadiri, H. Ahmadian, L. Martin de Juan, D. Xu, H. Tantawy, D.  
21 Smith, Impact attrition of spray-dried burkeite particles, *Powder Technol.* 304 (2016)  
22 2–7. doi:10.1016/j.powtec.2016.08.024.
- 23 [28] Z. Grof, M. Kohout, F. Štěpánek, Multi-scale simulation of needle-shaped particle  
24 breakage under uniaxial compaction, *Chem. Eng. Sci.* 62 (2007) 1418–1429.  
25 doi:10.1016/j.ces.2006.11.033.
- 26 [29] Z. Grof, C.M. Schoellhammer, P. Rajniak, F. Štěpánek, Computational and  
27 experimental investigation of needle-shaped crystal breakage, *Int. J. Pharm.* 407 (2011)  
28 12–20. doi:10.1016/j.ijpharm.2010.12.031.
- 29 [30] Y. Guo, C. Wassgren, B. Hancock, W. Ketterhagen, J. Curtis, Predicting breakage of  
30 high aspect ratio particles in an agitated bed using the Discrete Element Method, *Chem.*  
31 *Eng. Sci.* 158 (2017) 314–327. doi:10.1016/j.ces.2016.10.043.
- 32 [31] C.S. MacLeod, F.L. Muller, On the fracture of pharmaceutical needle-shaped crystals  
33 during pressure filtration: Case studies and mechanistic understanding, *Org. Process*  
34 *Res. Dev.* 16 (2012) 425–434. doi:10.1021/op200279m.
- 35 [32] R. Ho, M. Naderi, J.Y.Y. Heng, D.R. Williams, F. Thielmann, P. Bouza, A.R. Keith, G.  
36 Thiele, D.J. Burnett, Effect of milling on particle shape and surface energy heterogeneity  
37 of needle-Shaped crystals, *Pharm. Res.* 29 (2012) 2806–2816. doi:10.1007/s11095-012-  
38 0842-1.
- 39 [33] S. Antonyuk, S. Palis, S. Heinrich, Breakage behaviour of agglomerates and crystals by  
40 static loading and impact, *Powder Technol.* 206 (2011) 88–98.  
41 doi:10.1016/j.powtec.2010.02.025.
- 42 [34] M.T. Ruggiero, J. Sibik, J.A. Zeitler, T.M. Korter, Examination of l -Glutamic Acid  
43 Polymorphs by Solid-State Density Functional Theory and Terahertz Spectroscopy, *J.*

- 1 Phys. Chem. A. 120 (2016) 7490–7495. doi:10.1021/acs.jpca.6b05702.
- 2 [35] (2H)1,4-BENZOTHAZIN-3(4H)-ONE, Chemicalbook. (2019).  
3 [https://www.chemicalbook.com/ProductList\\_En.aspx?kwd=2H-1,4-Benzothiazin-](https://www.chemicalbook.com/ProductList_En.aspx?kwd=2H-1,4-Benzothiazin-3(4H)-One)  
4 3(4H)-One (accessed July 2, 2019).
- 5 [36] Potassium dihydrogen phosphate, Anhydrous, 99.995% Suprapur™, MilliporeSigma™,  
6 FisherScientific. (2019). [https://www.fishersci.com/shop/products/potassium-](https://www.fishersci.com/shop/products/potassium-dihydrogen-phosphate-anhydrous-99-995-suprapur-emd-millipore-2/M1051080050)  
7 dihydrogen-phosphate-anhydrous-99-995-suprapur-emd-millipore-2/M1051080050  
8 (accessed July 2, 2019).
- 9 [37] X.Z. Wang, J. Calderon De Anda, K.J. Roberts, Real-time measurement of the growth  
10 rates of individual crystal facets using imaging and image analysis: A feasibility study  
11 on needle-shaped crystals of L-glutamic acid, Chem. Eng. Res. Des. 85 (2007) 921–927.  
12 doi:10.1205/cherd06203.
- 13 [38] M. Mathew, W. Wong-Ng, Crystal structure of a new monoclinic form of potassium  
14 dihydrogen phosphate containing orthophosphacidium ion, [h 4 po 4 ] +1, J. Solid State  
15 Chem. 114 (1995) 219–223. doi:10.1006/jssc.1995.1031.
- 16 [39] M. Ali, M. Ghadiri, Analysis of triboelectric charging of particles due to aerodynamic  
17 dispersion by a pulse of pressurised air jet, Adv. Powder Technol. 28 (2017) 2735–2740.  
18 doi:10.1016/j.appt.2017.07.026.
- 19 [40] G.H. Ganser, A rational approach to drag prediction of spherical and nonspherical  
20 particles, Powder Technol. 77 (1993) 143–152. doi:10.1016/0032-5910(93)80051-B.
- 21 [41] W. P. Goh, M. Ali, K. Sinha, N.K. Nere, R. Ho, S. Bordawekar, A. Sheikh, M. Ghadiri,  
22 Assessment of Impact Breakage of Carbamazepine Dihydrate due to Aerodynamic  
23 Dispersion, (2019). Personal Communication.
- 24 [42] F.R. Menter, Y. Egorov, The Scale-Adaptive Simulation Method for Unsteady  
25 Turbulent Flow Predictions. Part 1: Theory and Model Description, Flow, Turbul.  
26 Combust. 85 (2010) 113–138. doi:10.1007/s10494-010-9264-5.

27

## 28 Appendix A. Supplementary Breakage Data

29

30 Table A1. Characteristic measures of the square-equivalent side length distribution by volume/area  $D_{10}$ ,  $D_{50}$  and  $D_{90}$  of the  
31 model test crystals for different dispersion pressures.

Material	Characteristic Size, $d_{SE}$ ( $\mu\text{m}$ )								
	$\beta$ L-glutamic acid			benzothiazin			potassium phosphate		
	Pressure (barg)	$D_{10}$	$D_{50}$	$D_{90}$	$D_{10}$	$D_{50}$	$D_{90}$	$D_{10}$	$D_{50}$
0.5	25	80	165	42	119	226	243	421	713
1	23	66	144	30	95	193	236	422	638
1.5	20	53	121	28	88	182	248	403	629
2	17	45	107	16	64	146	195	364	572
2.5	16	41	97	12	50	129	238	414	632
3	17	44	110	9	40	123	189	352	528

3.5	13	34	81	6	27	91	257	430	672
4	13	32	84	5	23	85	235	403	578
4.5	11	28	69	4	28	125	218	386	663
5	12	30	77	8	40	125	216	396	624

1

2

3 Table A2. Characteristic measures of particle length distribution by volume/area  $L_{10}$ ,  $L_{50}$  and  $L_{90}$  of the model test crystals  
4 for different dispersion pressures.

Material	Length, $L$ ( $\mu\text{m}$ )								
	$\beta$ L-glutamic acid			benzothiazin			potassium phosphate		
	Pressure (barg)	$L_{10}$	$L_{50}$	$L_{90}$	$L_{10}$	$L_{50}$	$L_{90}$	$L_{10}$	$L_{50}$
0.5	57	249	550	76	292	648	393	809	1450
1	46	171	468	51	216	525	390	827	1481
1.5	37	123	365	45	191	487	421	772	1321
2	29	89	290	24	124	374	307	673	1307
2.5	27	78	239	17	88	302	387	750	1353
3	27	85	296	13	66	291	290	659	1122
3.5	21	59	180	9	43	185	442	823	1335
4	20	56	208	7	35	168	375	764	1148
4.5	17	45	145	6	43	298	345	715	1205
5	18	49	158	11	71	302	352	750	1277

5

6

7 Table A3. Characteristic measures of particle width distribution by volume/area  $W_{10}$ ,  $W_{50}$  and  $W_{90}$  of the model test crystals  
8 for different dispersion pressures.

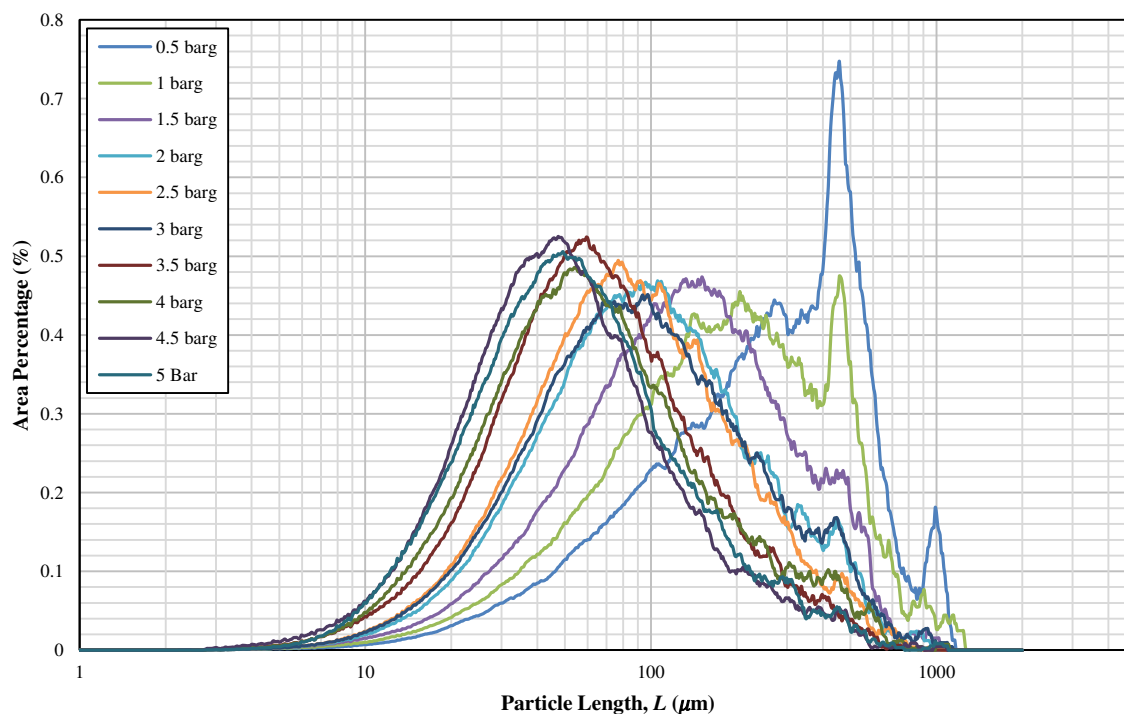
Material	Width, $W$ ( $\mu\text{m}$ )								
	$\beta$ L-glutamic acid			benzothiazin			potassium phosphate		
	Pressure (barg)	$W_{10}$	$W_{50}$	$W_{90}$	$W_{10}$	$W_{50}$	$W_{90}$	$W_{10}$	$W_{50}$
0.5	13	30	67	26	60	110	196	338	555
1	13	29	64	21	52	99	192	325	487
1.5	12	28	62	20	49	93	199	319	490
2	12	27	61	14	41	81	166	300	446
2.5	11	27	60	10	35	77	195	323	496
3	12	29	65	8	30	72	161	285	434
3.5	11	25	56	6	23	60	209	338	525
4	10	24	53	5	20	58	196	317	439
4.5	10	23	49	5	22	70	182	310	532
5	10	24	55	7	29	72	179	313	481

1  
2  
3  
4

Table A4. Characteristic measures of particle aspect ratio distribution by volume/area  $AR_{10}$ ,  $AR_{50}$  and  $AR_{90}$  of the model test crystals for different dispersion pressures.

Material	Aspect Ratio, $AR$ (-)								
	$\beta$ L-glutamic acid			benzothiazin			potassium phosphate		
	$AR_{10}$	$AR_{50}$	$AR_{90}$	$AR_{10}$	$AR_{50}$	$AR_{90}$	$AR_{10}$	$AR_{50}$	$AR_{90}$
Pressure (barg)									
0.5	0.07	0.13	0.34	0.12	0.21	0.47	0.28	0.41	0.65
1	0.08	0.18	0.46	0.14	0.25	0.56	0.25	0.38	0.66
1.5	0.10	0.23	0.56	0.14	0.26	0.59	0.28	0.40	0.69
2	0.12	0.33	0.67	0.16	0.34	0.73	0.28	0.43	0.71
2.5	0.13	0.37	0.71	0.19	0.43	0.77	0.28	0.43	0.69
3	0.12	0.37	0.71	0.19	0.47	0.81	0.30	0.44	0.72
3.5	0.17	0.47	0.78	0.24	0.56	0.84	0.29	0.40	0.64
4	0.15	0.48	0.79	0.26	0.60	0.86	0.30	0.40	0.69
4.5	0.20	0.55	0.81	0.19	0.55	0.86	0.31	0.43	0.72
5	0.21	0.54	0.81	0.18	0.44	0.81	0.31	0.43	0.67

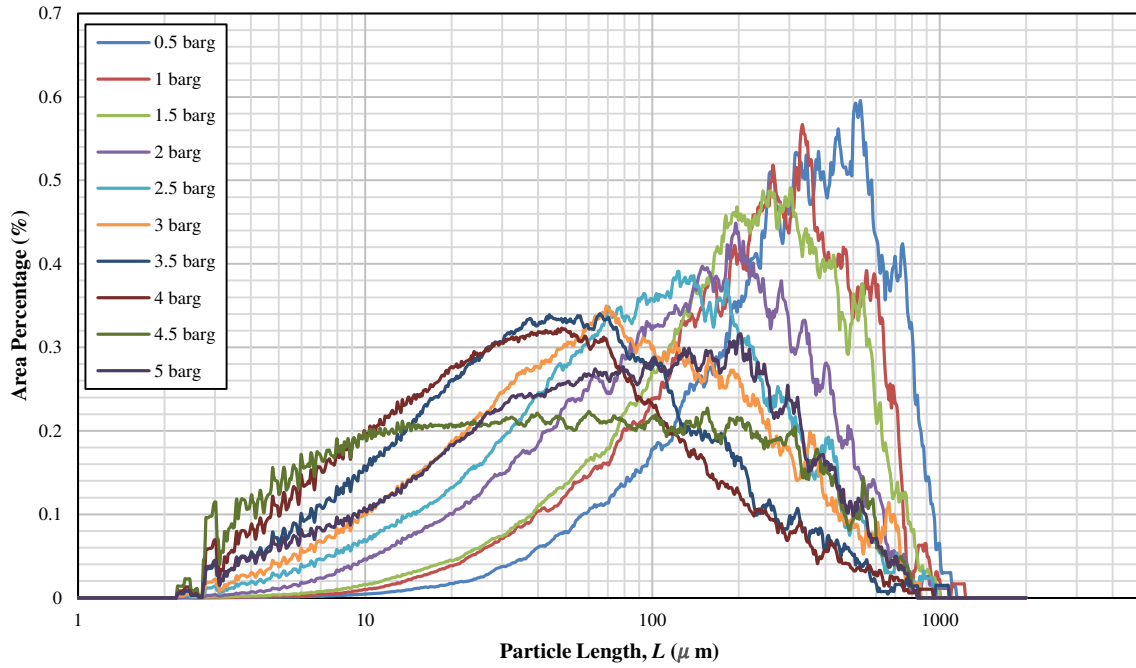
5  
6



7  
8  
9

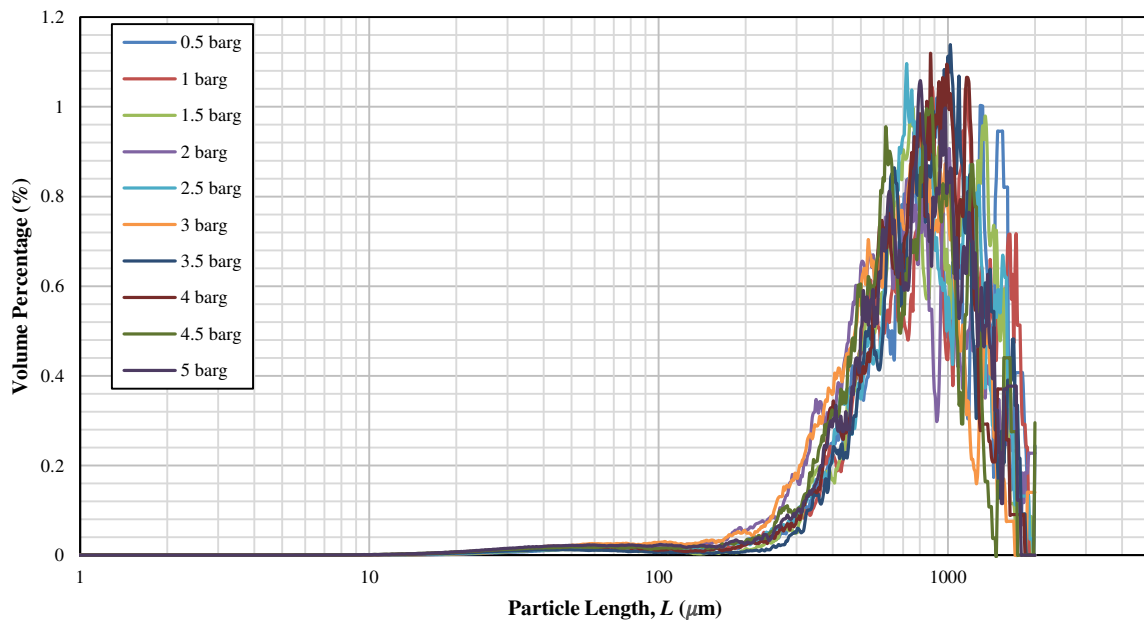
Fig. A1. Area percentage distribution of particle length for  $\beta$  L-glutamic acid samples dispersed by 0.5, 1, 1.5, 2, 2.5, 3, 3.5, 4, 4.5 and 5 barg pressures.

10



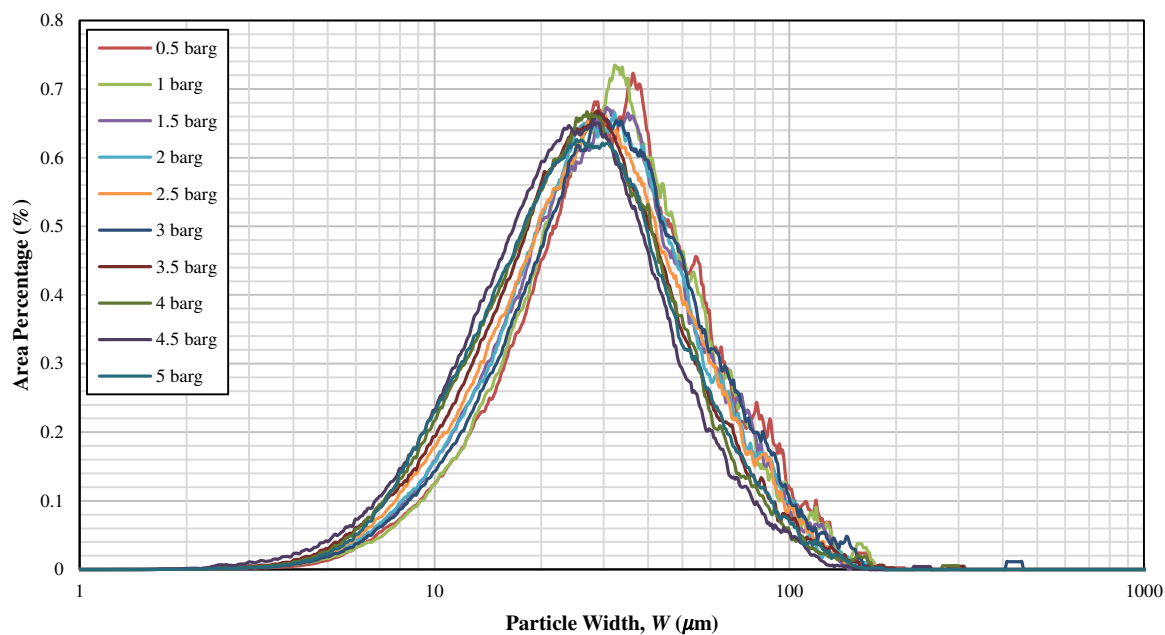
1  
2  
3  
4

Fig. A2. Area percentage distribution of particle length for benzothiazin samples dispersed by 0.5, 1, 1.5, 2, 2.5, 3, 3.5, 4, 4.5 and 5 barg pressures.

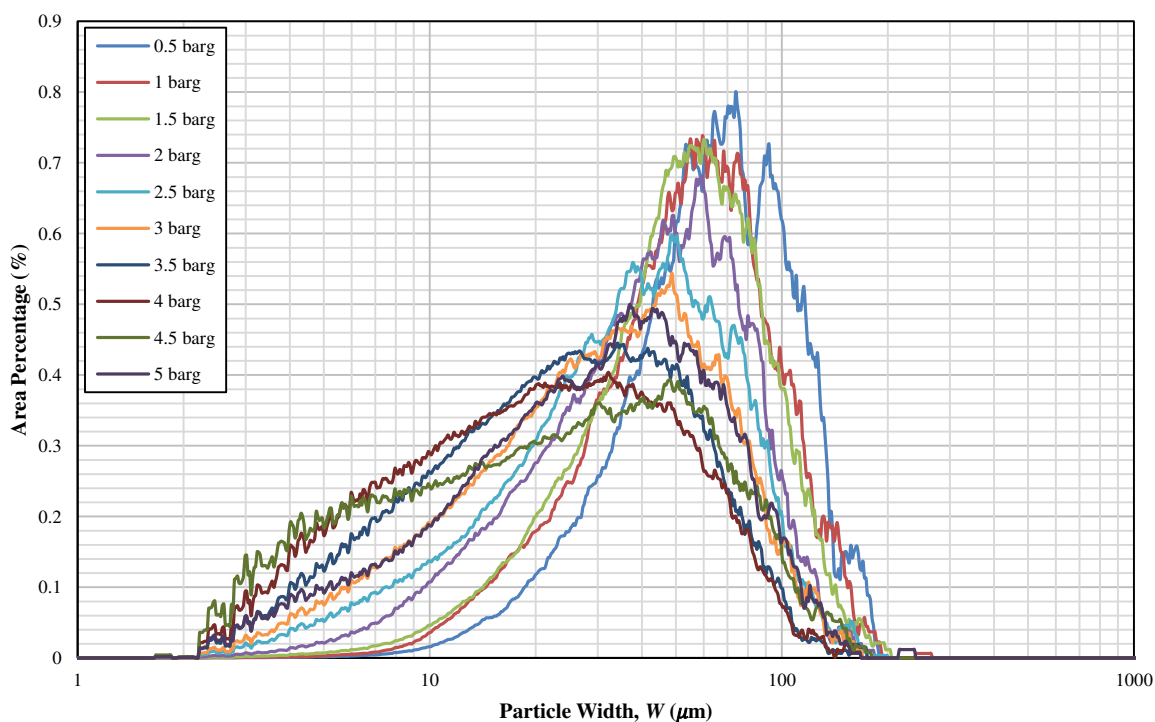


5  
6  
7  
8

Fig. A3. Volume percentage distribution of particle length for potassium phosphate samples dispersed by 0.5, 1, 1.5, 2, 2.5, 3, 3.5, 4, 4.5 and 5 barg pressures.

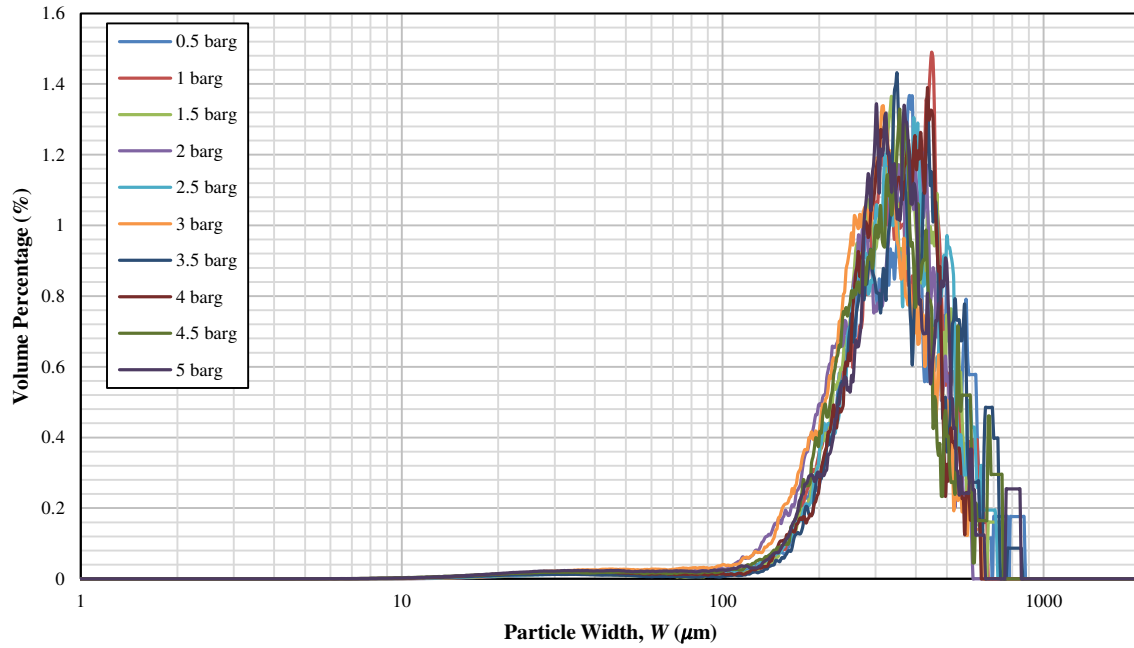


1  
 2 Fig. A4. Area percentage distribution of particle width for  $\beta$  L-glutamic acid samples dispersed by 0.5, 1, 1.5, 2, 2.5, 3, 3.5,  
 3 4, 4.5 and 5 barg pressures.



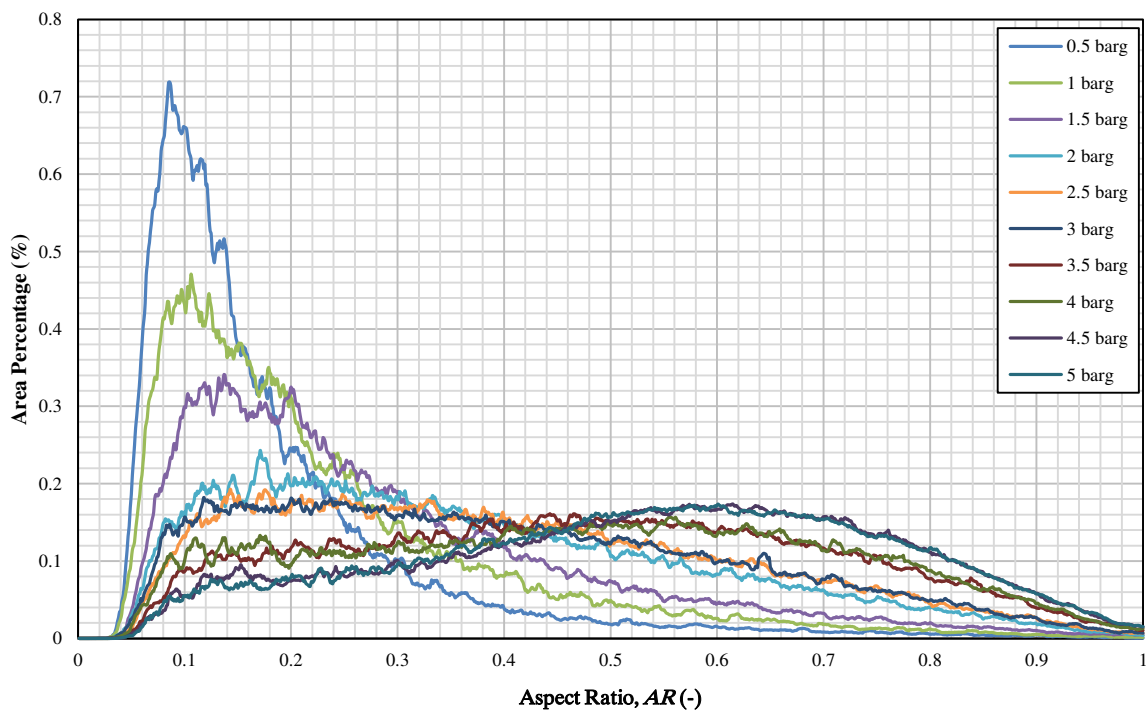
5  
 6 Fig. A5. Area percentage distribution of particle width for benzothiazin samples dispersed by 0.5, 1, 1.5, 2, 2.5, 3, 3.5, 4, 4.5  
 7 and 5 barg pressures.

8



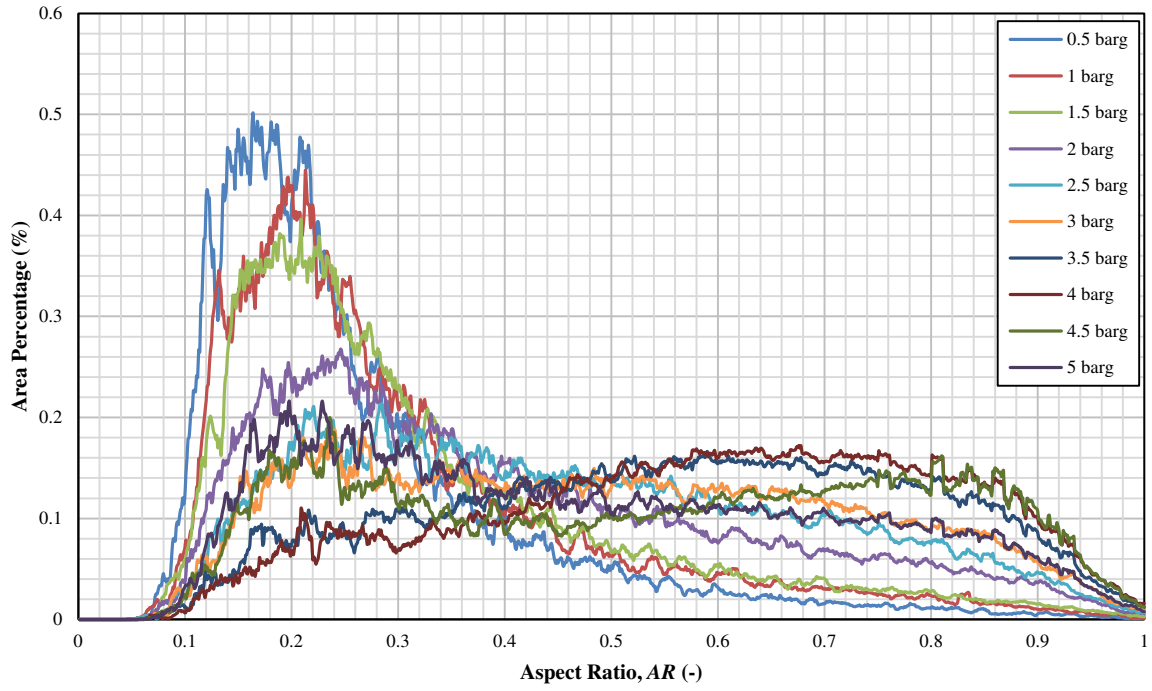
1  
 2 Fig. A6. Volume percentage distribution of particle width for potassium phosphate samples dispersed by 0.5, 1, 1.5, 2, 2.5, 3,  
 3 3.5, 4, 4.5 and 5 barg pressures.

4



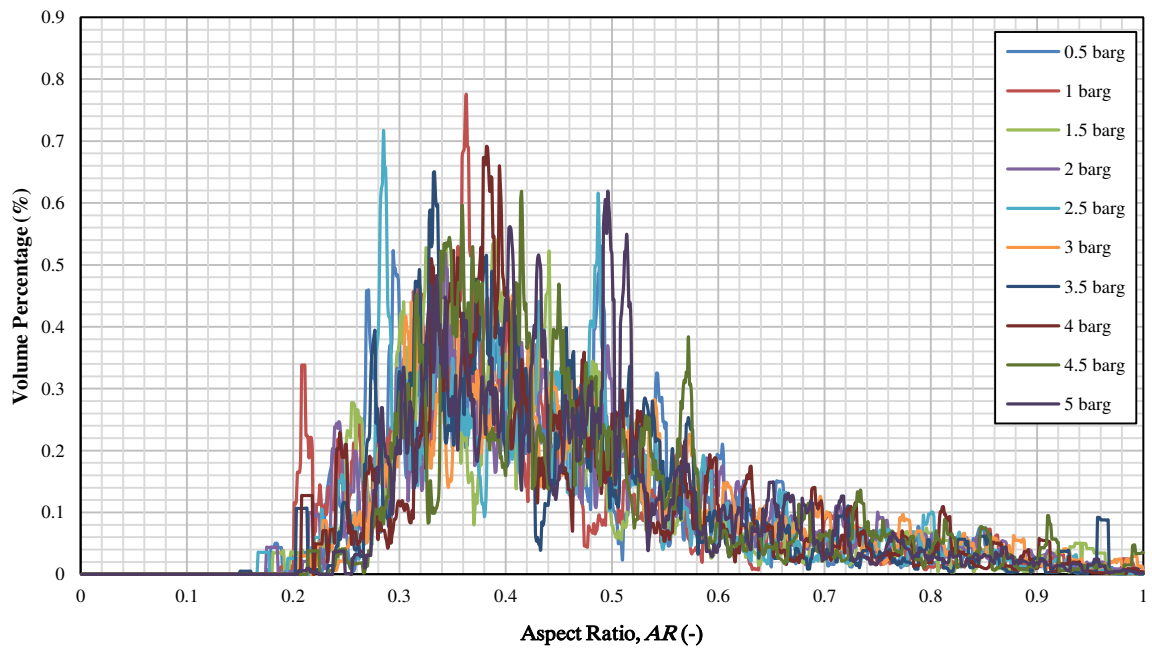
5  
 6 Fig. A7. Area percentage distribution of particle aspect ratio for  $\beta$  L-glutamic acid samples dispersed by 0.5, 1, 1.5, 2, 2.5, 3,  
 7 3.5, 4, 4.5 and 5 barg pressures.

8



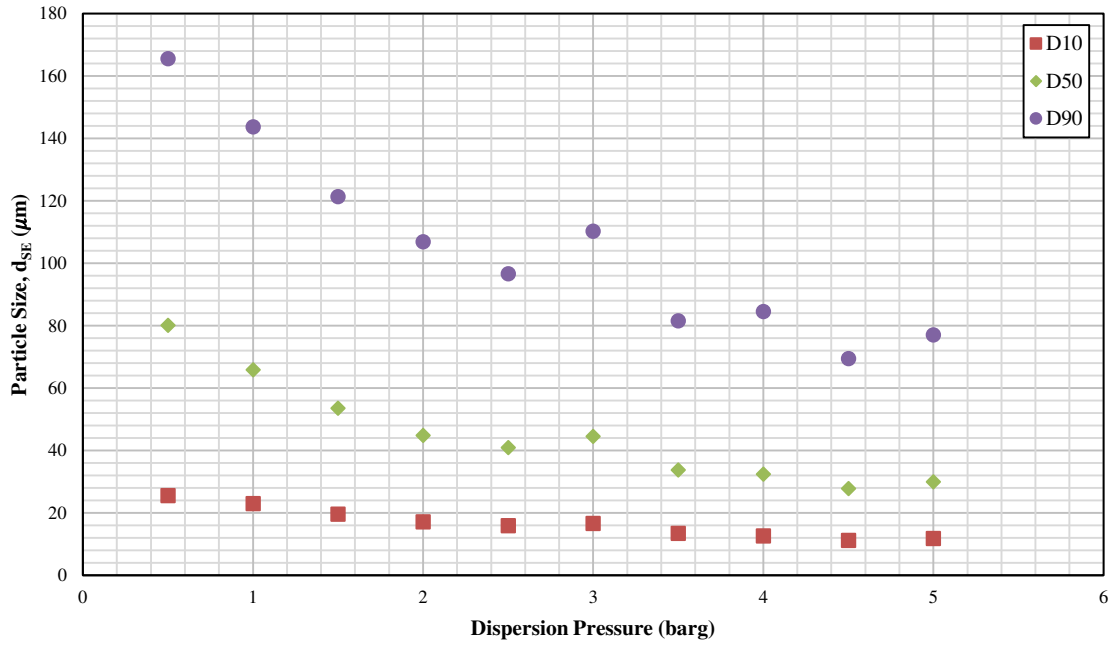
1  
 2 Fig. A8. Area percentage distribution of particle aspect ratio for benzothiazin samples dispersed by 0.5, 1, 1.5, 2, 2.5, 3, 3.5,  
 3 4, 4.5 and 5 barg pressures.

4



5  
 6 Fig. A9. Volume percentage distribution of particle aspect ratio for potassium phosphate samples dispersed by 0.5, 1, 1.5, 2,  
 7 2.5, 3, 3.5, 4, 4.5 and 5 barg pressures.

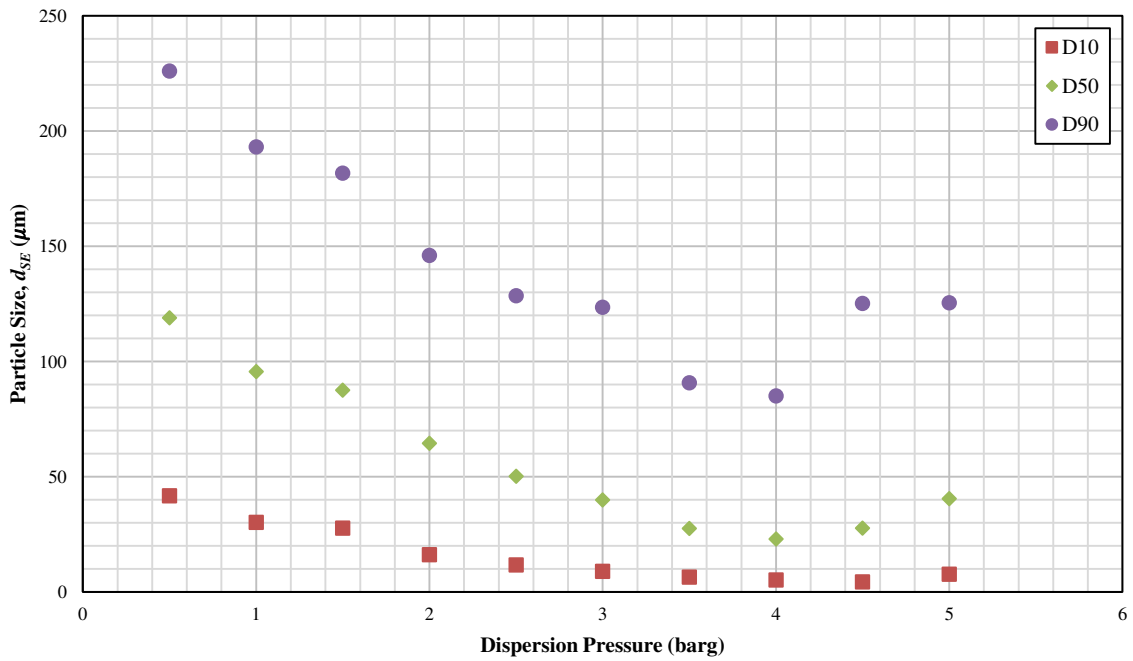
8



1

2 Fig. A10. Characteristic measures of the square-equivalent side length distribution by area  $D_{10}$ ,  $D_{50}$  and  $D_{90}$  for  $\beta$  L-glutamic  
3 acid crystals as a function of dispersion pressure.

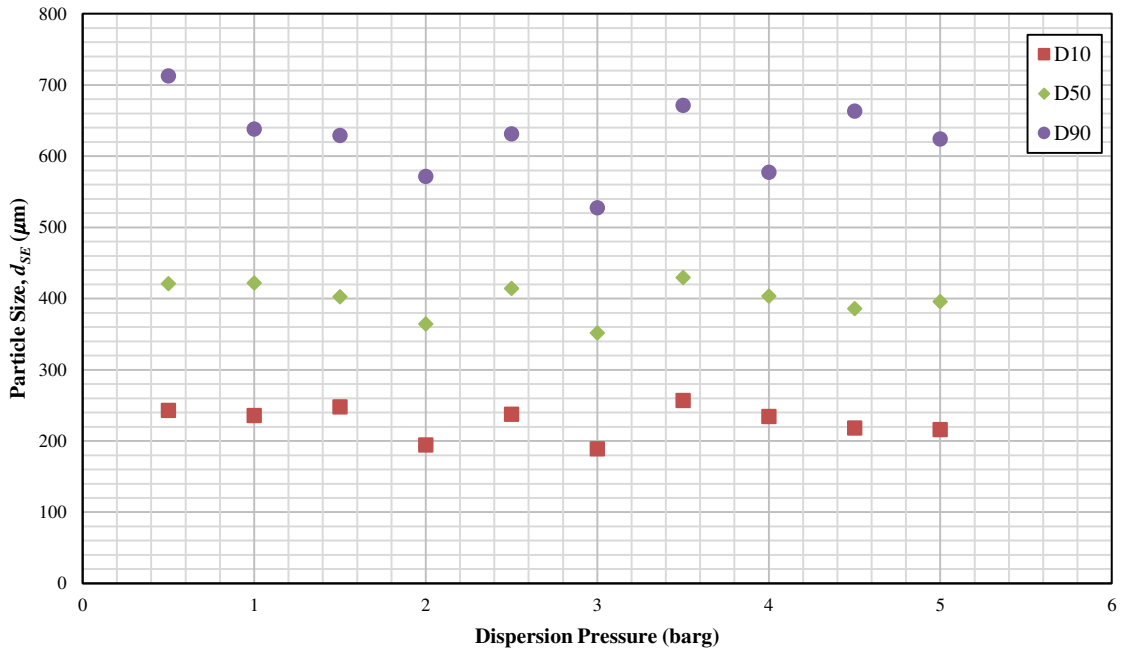
4



5

6 Fig. A11. Characteristic measures of the square-equivalent side length distribution by area  $D_{10}$ ,  $D_{50}$  and  $D_{90}$  for benzothiazin  
7 crystals as a function of dispersion pressure.

1

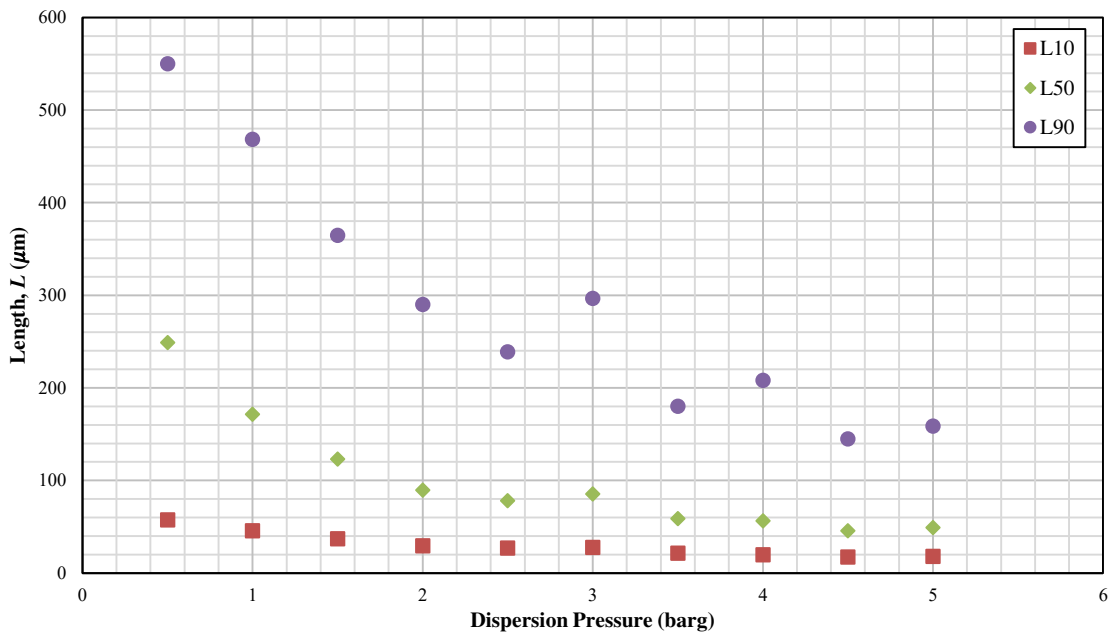


2

3 Fig. A12. Characteristic measures of the square-equivalent side length distribution by volume  $D_{10}$ ,  $D_{50}$  and  $D_{90}$  for potassium  
4 phosphate crystals as a function of dispersion pressure.

5

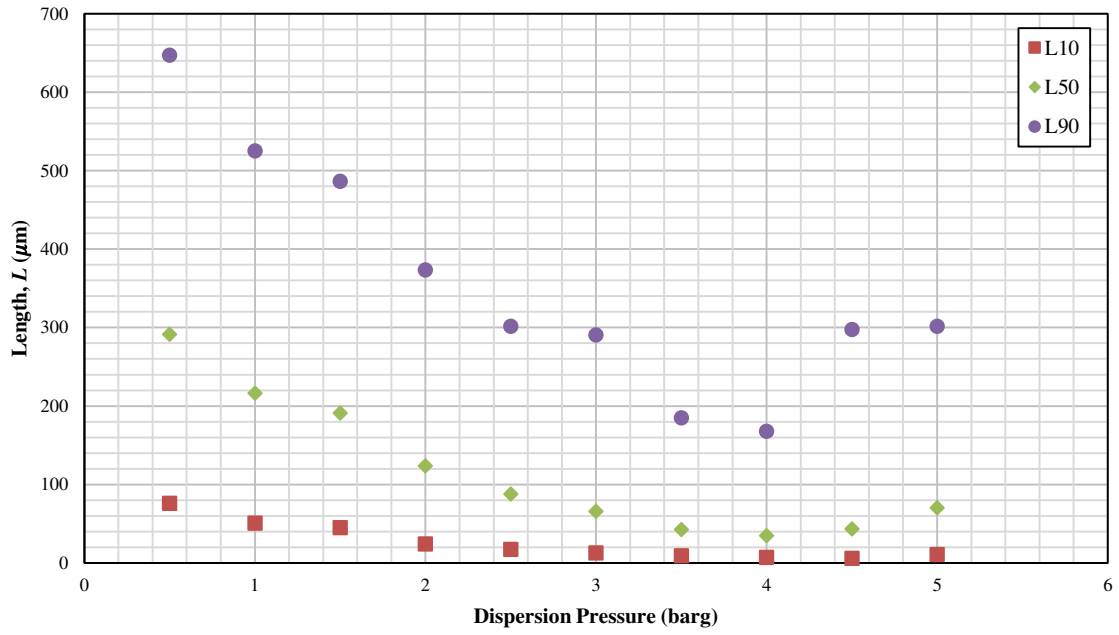
6



7

8 Fig. A13. Characteristic measures of particle length distribution by area  $L_{10}$ ,  $L_{50}$  and  $L_{90}$  for  $\beta$  L-glutamic acid crystals as a  
9 function of dispersion pressure.

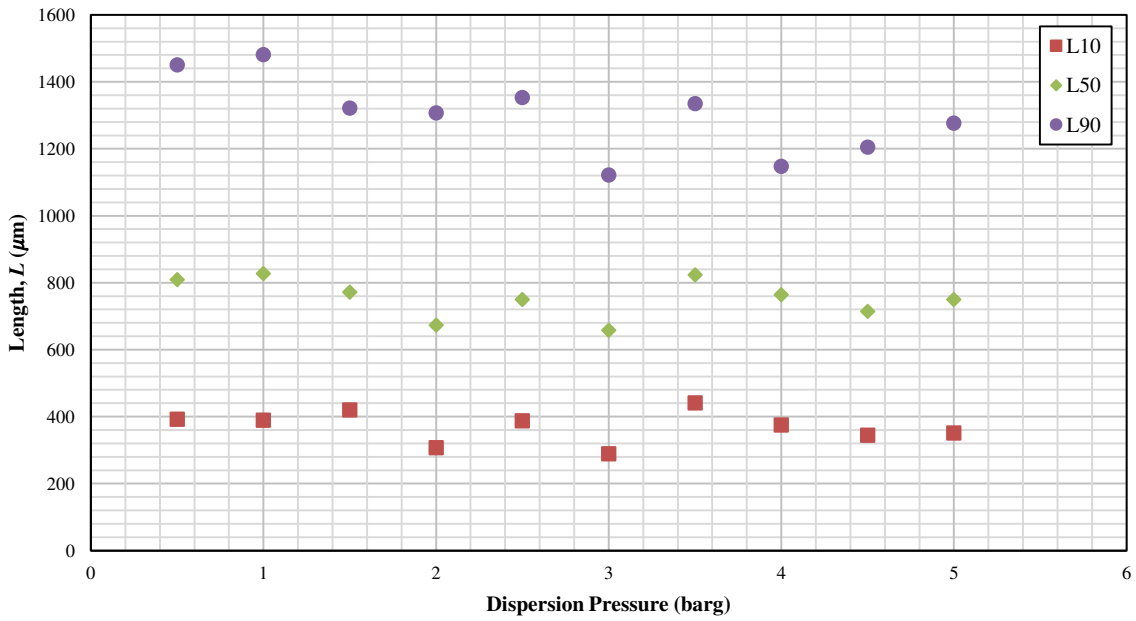
1



2

3 Fig. A14. Characteristic measures of particle length distribution by area  $L_{10}$ ,  $L_{50}$  and  $L_{90}$  for benzothiazin crystals as a  
4 function of dispersion pressure.

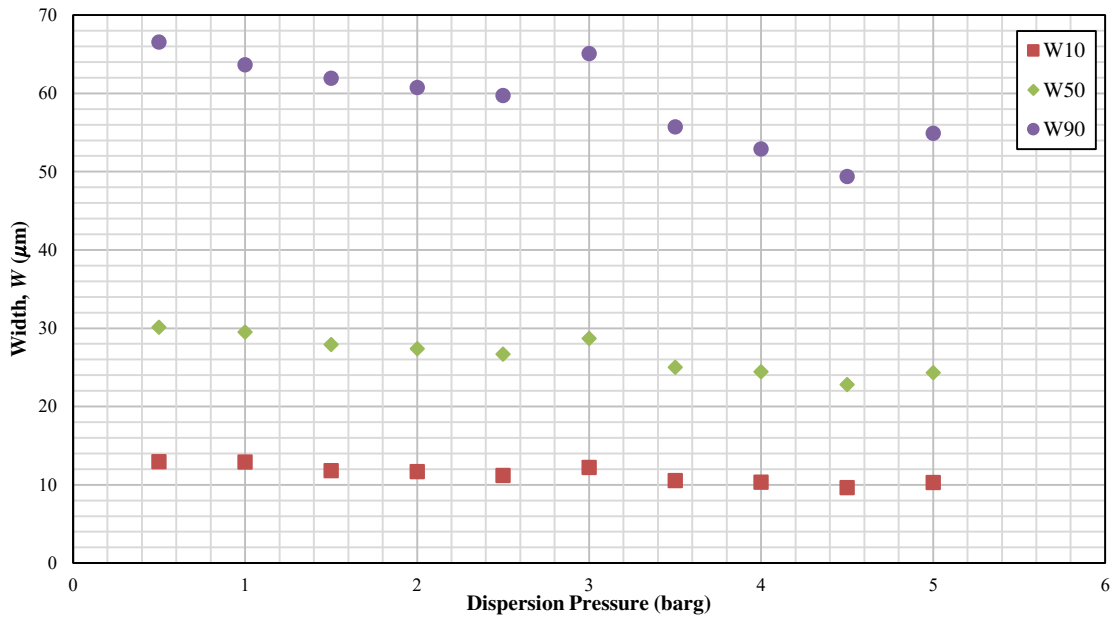
5



6

7 Fig. A15. Characteristic measures of particle length distribution by volume  $L_{10}$ ,  $L_{50}$  and  $L_{90}$  for potassium phosphate crystals  
8 as a function of dispersion pressure.

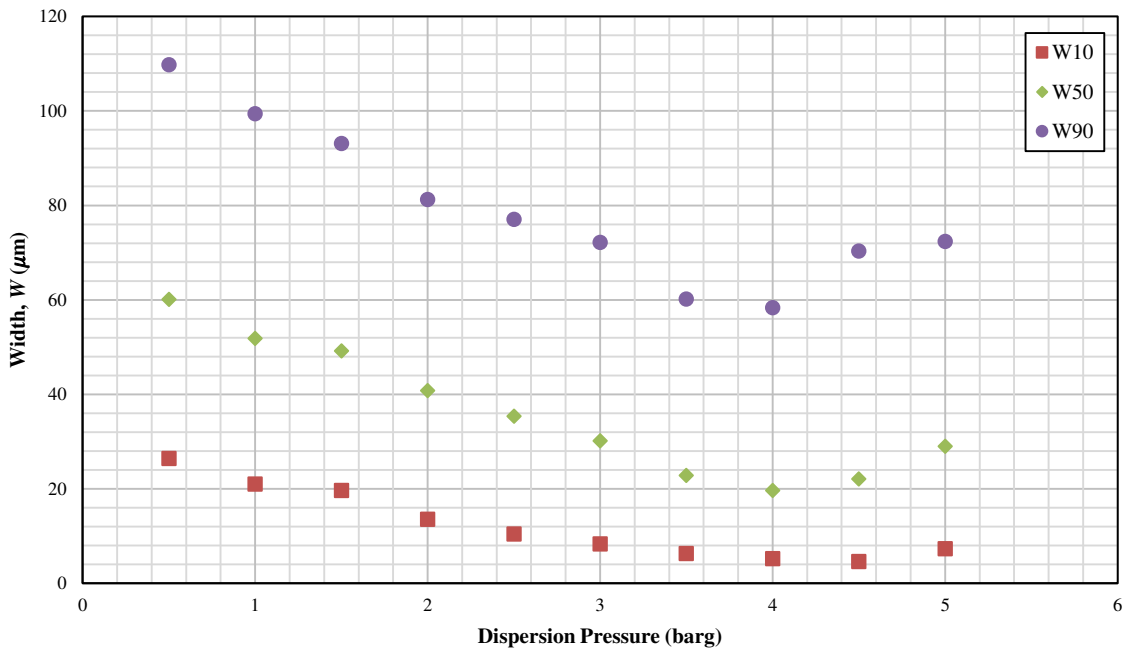
1



2

3 Fig. A16. Characteristic measures of particle width distribution by area  $W_{10}$ ,  $W_{50}$  and  $W_{90}$  for  $\beta$  L-glutamic acid crystals as a  
4 function of dispersion pressure.

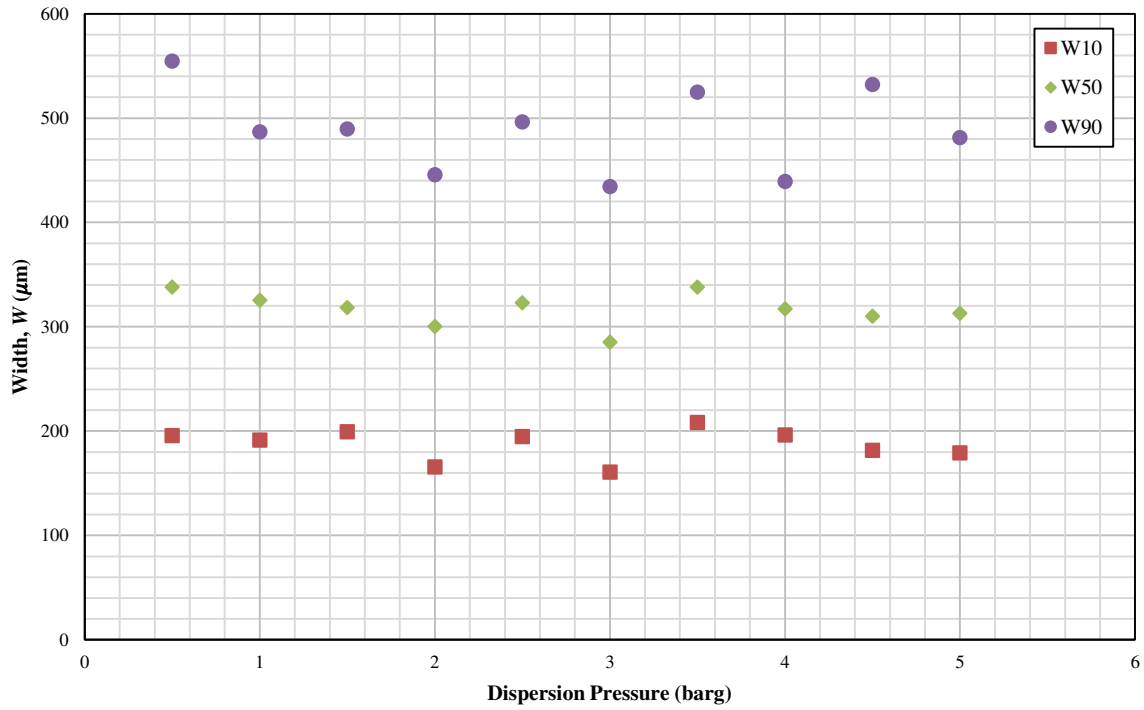
5



6

7 Fig. A17. Characteristic measures of particle width distribution by area  $W_{10}$ ,  $W_{50}$  and  $W_{90}$  for benzothiazin crystals as a  
8 function of dispersion pressure.

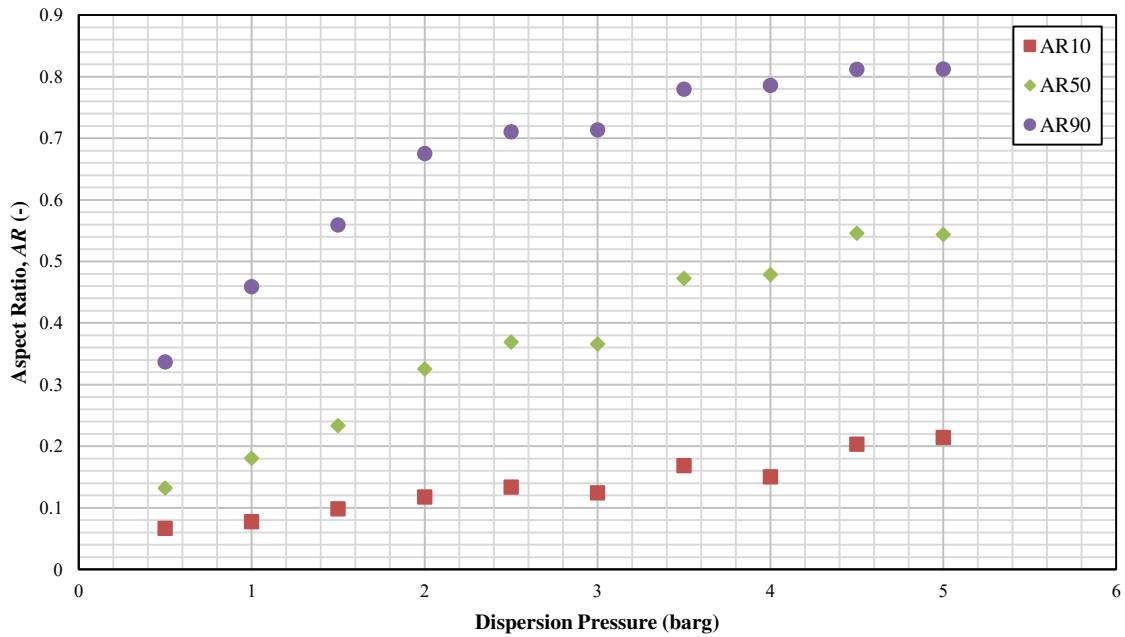
1



2

3 Fig. A18. Characteristic measures of particle width distribution by volume  $W_{10}$ ,  $W_{50}$  and  $W_{90}$  for potassium phosphate  
4 crystals as a function of dispersion pressure.

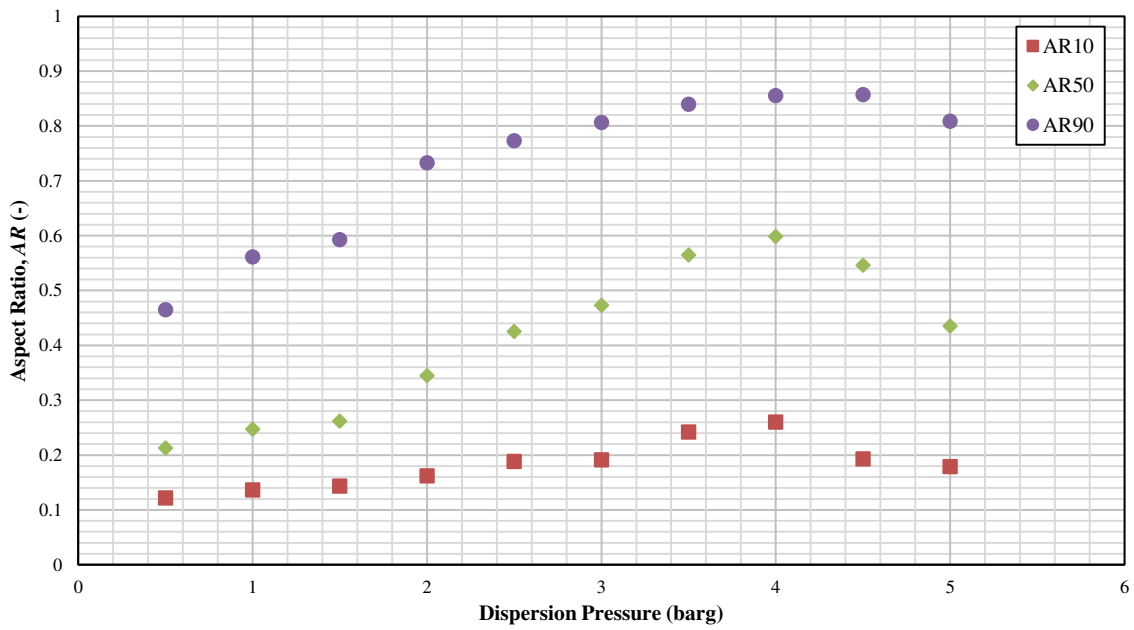
5



6

7 Fig. A19. Characteristic measures of particle aspect ratio distribution by area  $AR_{10}$ ,  $AR_{50}$  and  $AR_{90}$  for  $\beta$  L-glutamic acid  
8 crystals as a function of dispersion pressure.

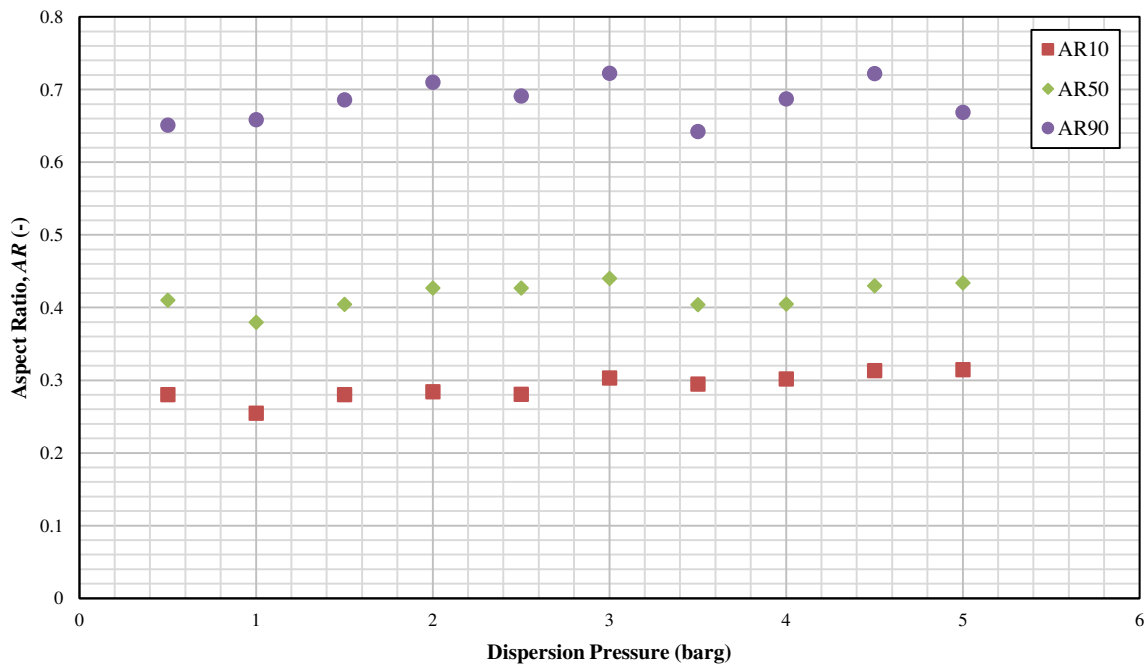
1



2

3 Fig. A20. Characteristic measures of particle aspect ratio distribution by area  $AR_{10}$ ,  $AR_{50}$  and  $AR_{90}$  for benzothiazin crystals  
4 as a function of dispersion pressure.

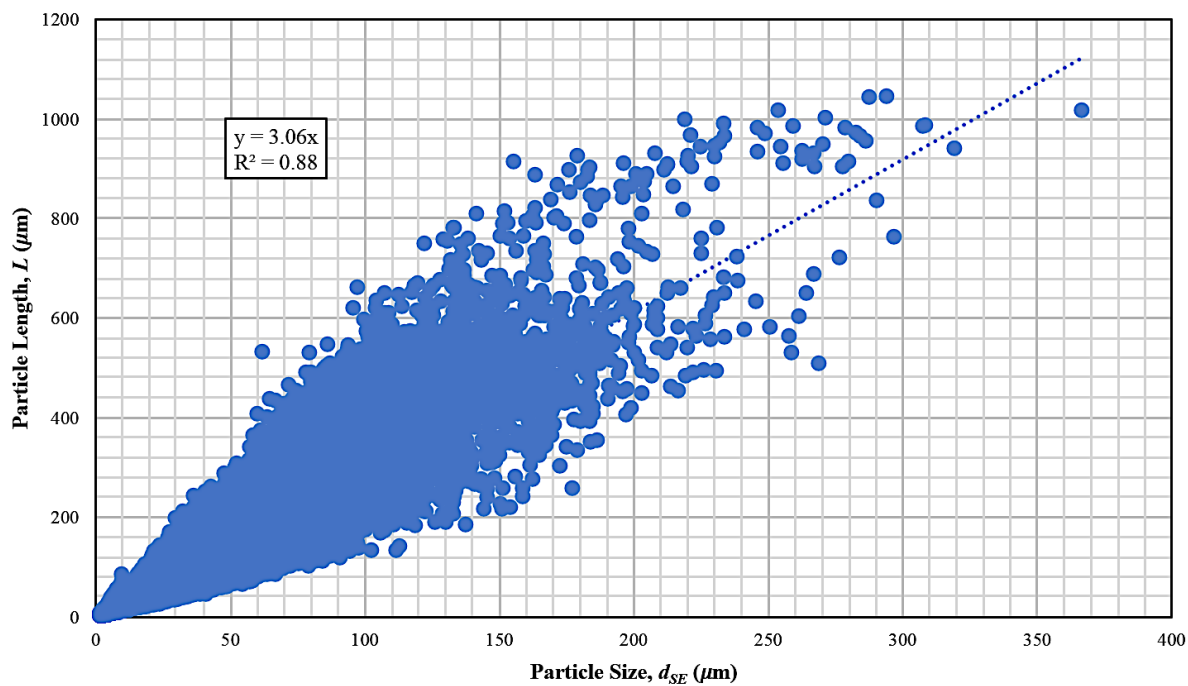
5



6

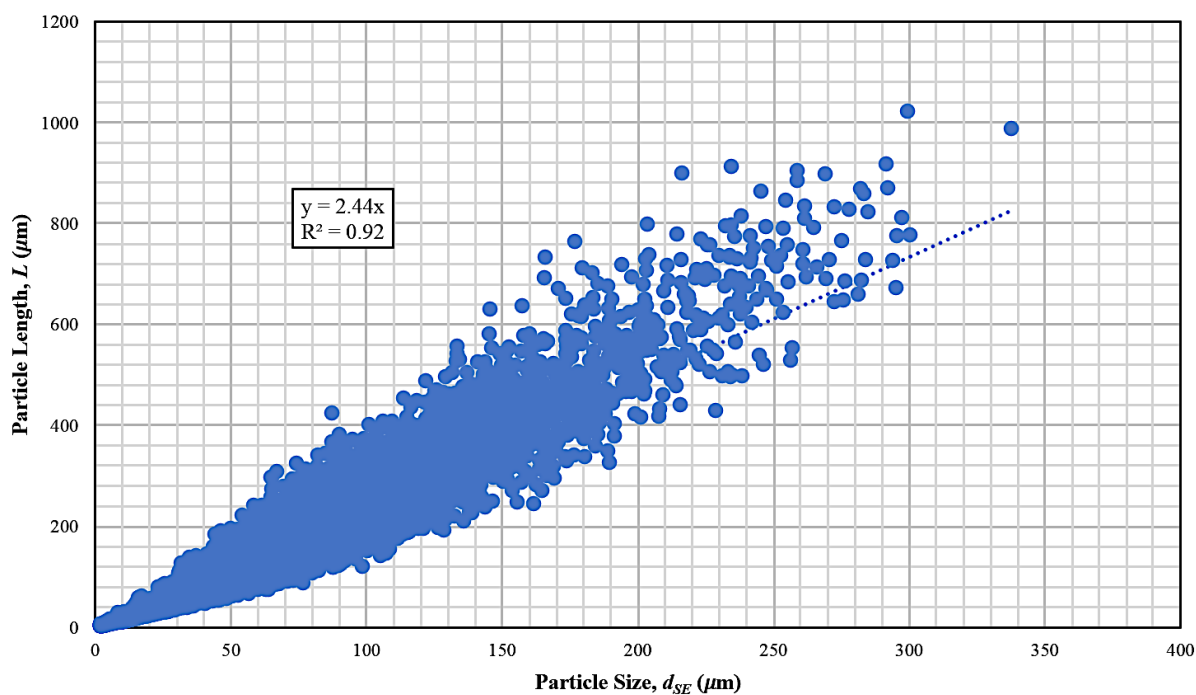
7 Fig. A21. Characteristic measures of particle aspect ratio distribution by volume  $AR_{10}$ ,  $AR_{50}$  and  $AR_{90}$  for potassium  
8 phosphate crystals as a function of dispersion pressure.

9



1  
2 Fig. A22. Particle length vs. particle size of  $\beta$  L-glutamic acid reference crystals (0.5 barg measurement) with  $k$  as the slope.

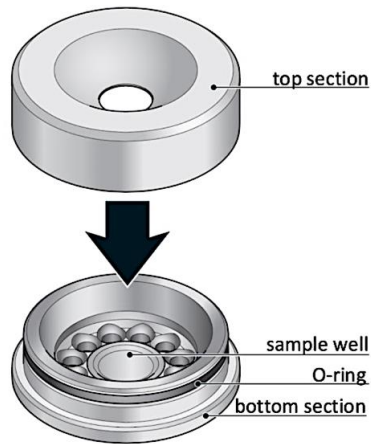
3



4  
5 Fig. A23. Particle length vs. particle size of benzothiazin reference crystals (0.5 barg measurement) with  $k$  as the slope.

1 Appendix B. Supplementary CFD Data

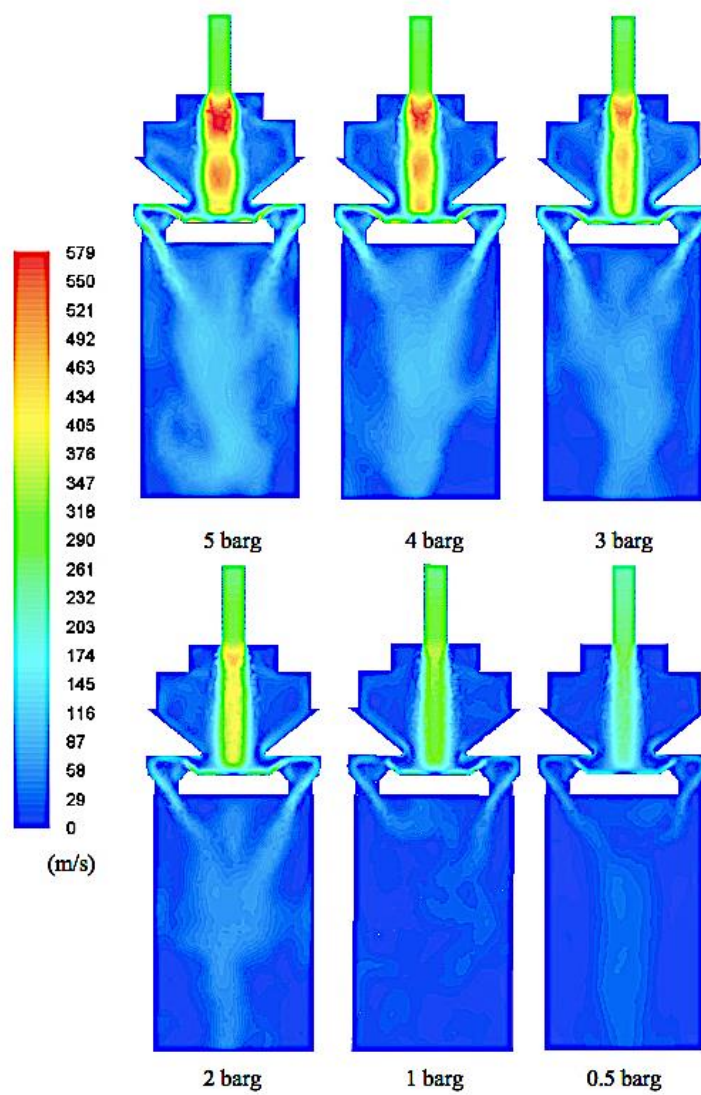
2  
3



4  
5

Fig. B1. Morphologi G3 dispersion spool (courtesy of Malvern Panalytical Ltd.).

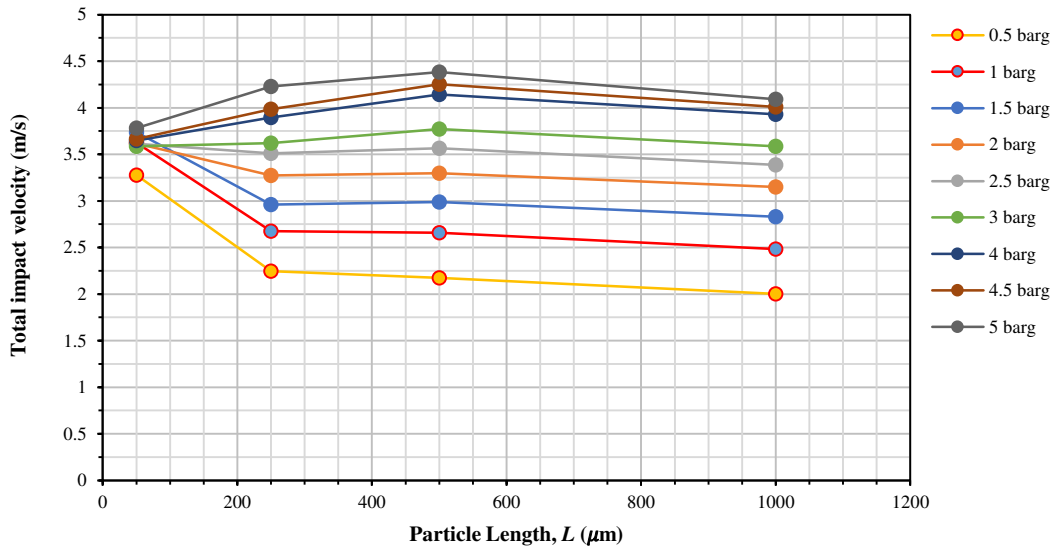
6



7  
8

Fig. B2. Air velocity contours at different inlet air pressures.

1

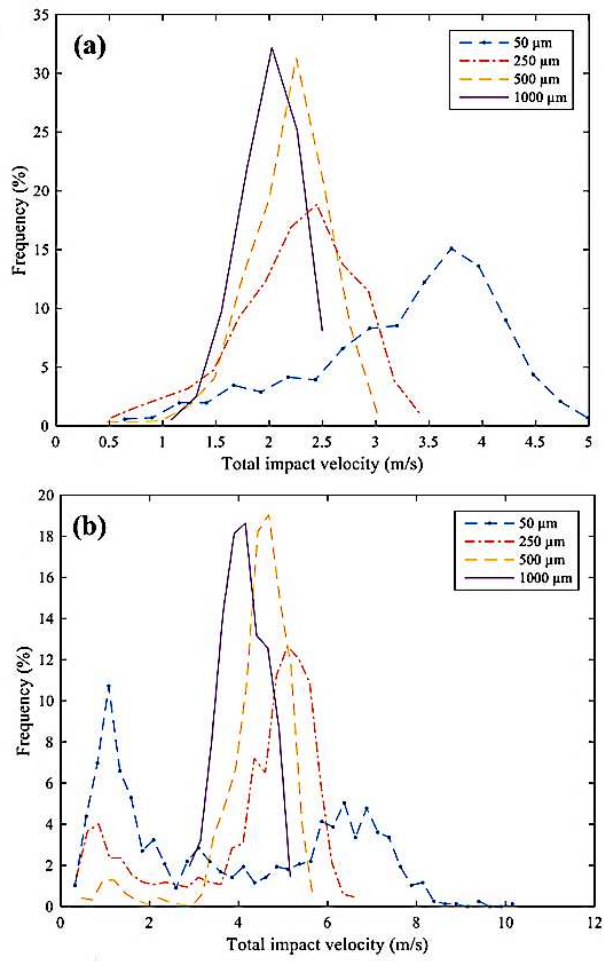


2

3

Fig. B3. Average total impact velocity of  $\beta$  L-glutamic acid crystals of different sizes at different inlet air pressures.

4



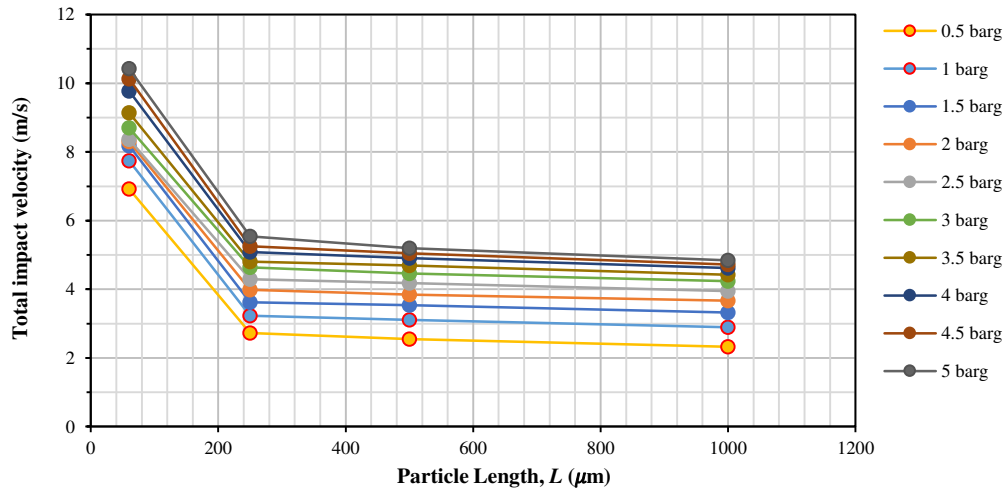
5

6

7

Fig. B4. Distribution of impact velocities of  $\beta$  L-glutamic acid crystals of different lengths. (a): 0.5 barg inlet pressure; (b): 5 barg inlet pressure.

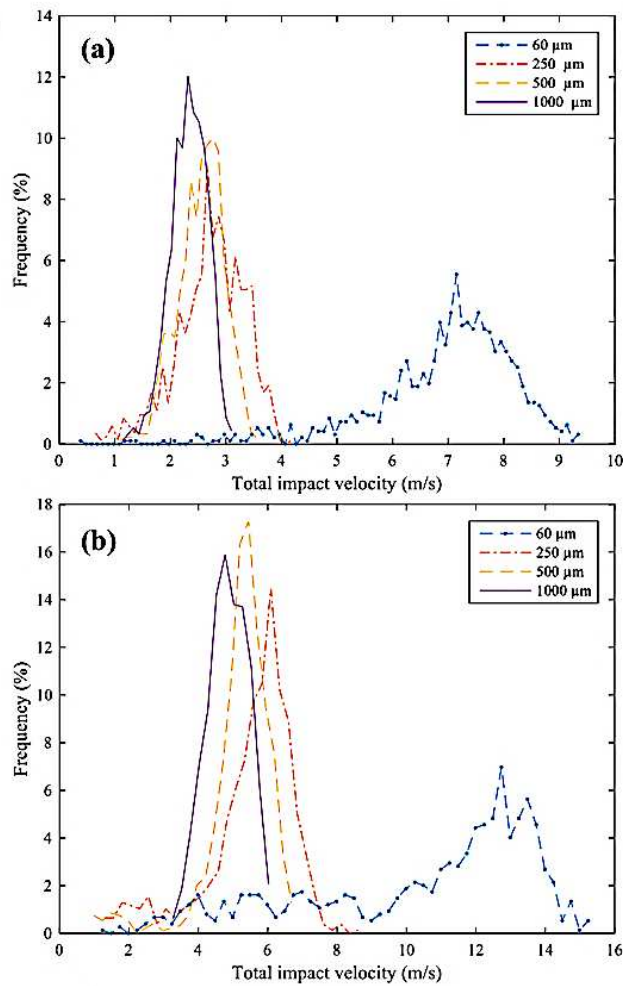
1



2

3

Fig. B5. Average total impact velocity of benzothiazin crystals of different sizes at different inlet air pressures.



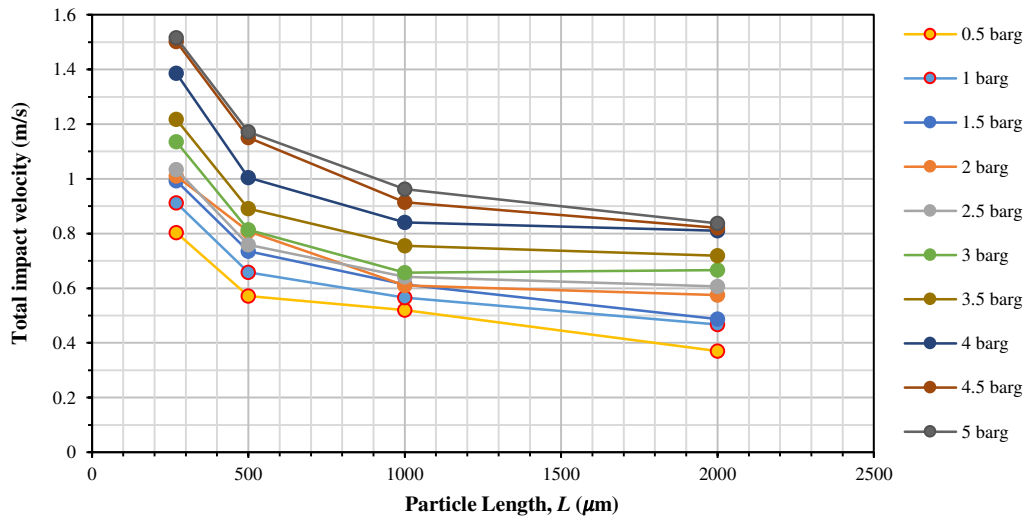
4

5

6

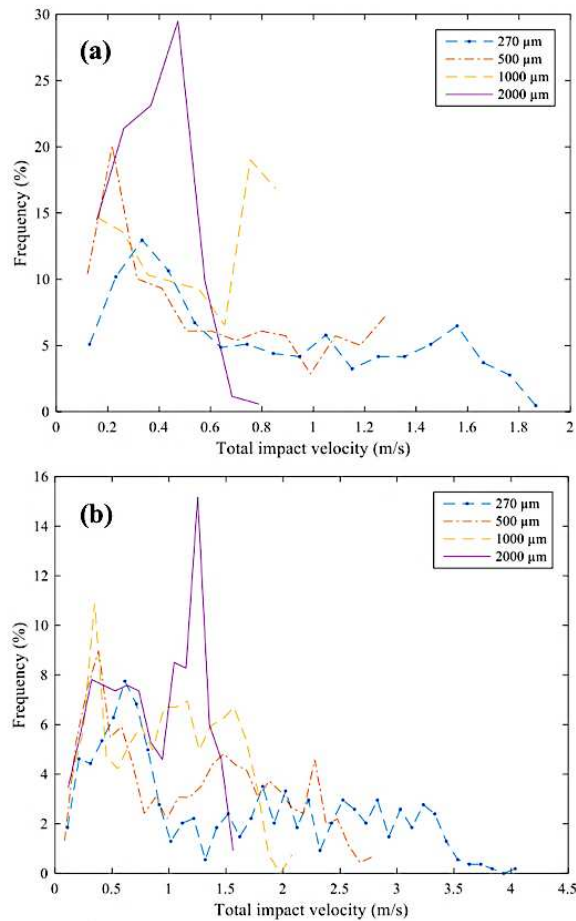
Fig. B6. Distribution of impact velocities of benzothiazin crystals of different lengths. (a): 0.5 barg inlet pressure; (b): 5 barg inlet pressure.

7



1  
2 Fig. B7. Average total impact velocity of potassium phosphate crystals of different sizes at different inlet air pressures.

3



4  
5 Fig. B8. Distribution of impact velocities of potassium phosphate crystals of different lengths. (a): 0.5 barg inlet pressure;  
6 (b): 5 barg inlet pressure.